Chapter-3

Niobate Based Double Perovskite Phosphors: Synthesis and Luminescence Investigation

Highlights

The present chapter describes a study on the effect of Eu^{3+} dopant on PL and TL properties of Sr_2YNbO_6 double perovskite phosphor. Total six samples of Sr_2YNbO_6 double perovskite were prepared, in which the concentration of Eu^{3+} dopant was taken in the range of 1 mol% to 5 mol%. The synthesis of all the phosphor compositions was accomplished through the combustion process, where in urea used as flux. After combustion, the received white powder then transfer to alumina crucible and heated at 1200 °C for six hours in open air in muffle furnace. The study ascribed various characterization techniques, including XRD, FESEM, FTIR, PL, temperature dependent PL, and TL after irradiating the phosphor by beta ionizing radiation. These techniques are standard, and were used to confirm the crystal structure of compound (XRD), examine the surface morphology (SEM), and to assess the material for the applications in LED and thermoluminescence dosimetry (TLD).

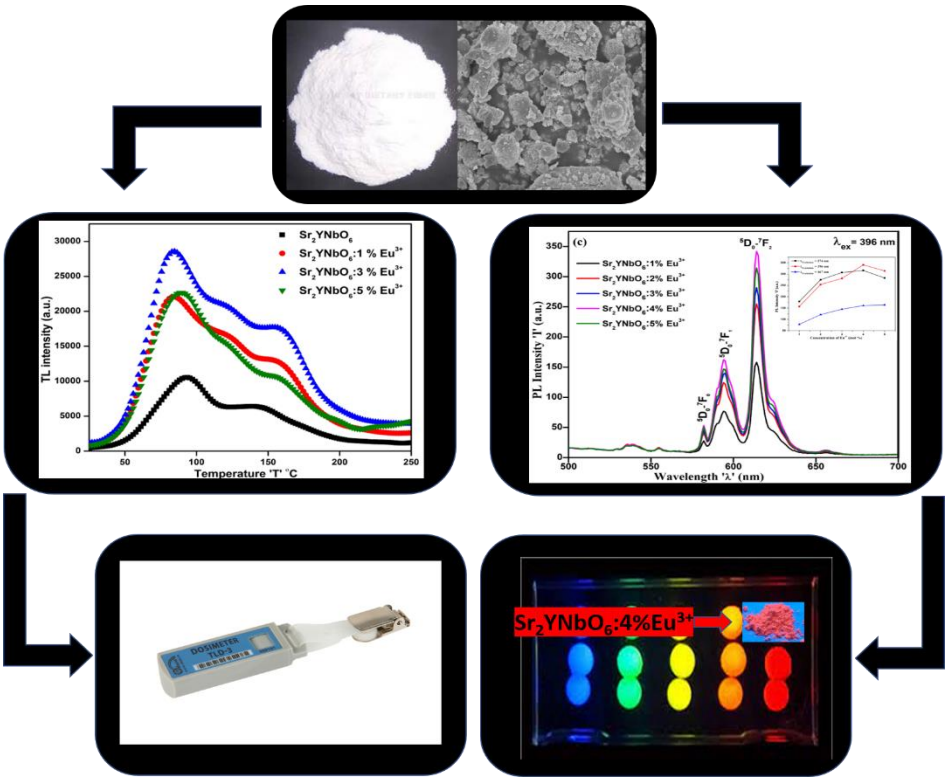

3.1 Introduction

The research interest in the potential luminescent materials has grown significantly in recent studies due to their promising applications in lighting devices. Recently, WLEDs have received substantial consideration as new-generation illumination devices due to their exceptional efficiency, long life (approximately 80000 burning hour), compact size, extended decay time, eco-friendliness, and reduced energy consumption compared to traditional fluorescent and incandescent lamps [1,2]. The present trend in phosphor-based WLEDs is using UV-LED chip (300-400 nm) and blue LED chip (467 nm) along with encapsulated phosphors (Red, Blue, Green, Yellow), to get high luminous intensity [3,4]. Combining B-R-G phosphors gives better CRI, which is more than 95%. The higher CRI can be achieved by increasing the red-component phosphor, and to improve the lumen per watt, the green-component phosphor plays a major role. By adjusting green and red component phosphors, the required color temperature can be achieved. The need of the day is to develop high CRI red component phosphor with extraordinary chemical and physical stability and high luminous efficiency, which became necessary to address the current requirements.

Herein, we reported the luminescence properties and functional applications of double perovskite composition Sr_2YNbO_6 (SYN) as a host doped with Eu^{3+} for solid-state lighting. Perovskite oxides with wide bandgap are promising candidates for investigating luminescence properties through rare earth doping for LED application. Moreover, the excellent chemical and thermal stability of oxide perovskites makes them a convincing choice as a host matrix for studying optical properties. During literature survey, quite a few double perovskites activated with lanthanides were reported for their fascinating photoluminescence properties. Whereas, the thermoluminescence in double perovskites received less attention. Very few papers on the TL study of double perovskites were found, as per the literature survey. It is interesting to investigate the double perovskites for their TL characterization.

The prepared series of $Sr_2YNbO_6:Eu^{3+}$ samples demonstrated excellent red down-conversion luminescence upon different excitations and temperature situations with notable color purity. Moreover, the impact of europium doping level on structural modifications and luminous properties was studied in a prepared series of phosphors. The significance of the phosphor's photoluminescence emission was assessed through thermal stability and PL decay lifetime measurements. Additionally, the thermoluminescence of the phosphor system was examined

subsequently after irradiating with a ^{90}Sr beta radiation source to assess the dosimetry aspects. The TL results revealed high sensitivity at smaller doses, displaying a linear dose response to the beta radiation. An excellent thermal stability and linear TL dose response to beta rays demonstrate the potential application of the phosphor in LED and TLD. From the overall results received from structural and luminescence characterization, the expected target to explore the double perovskite for TL studied was accomplished.

3.2 Synthesis Method and Characterization Techniques

3.2.1 Phosphor Preparation

In this study, a total 6 samples of Sr_2YNbO_6:x mol% Eu^{3+} (x=1.0-5.0) double perovskite phosphors, including base, were prepared through high-temperature combustion synthesis. To synthesize the phosphor materials, analytical reagent (AR) grade strontium nitrate [$Sr(NO_3)_2$, 99.5%, pure], yttrium oxide (Y_2O_3, 99.9% pure), niobium pentoxide (Nb_2O_5, 99.9% pure), and europium oxide (Eu_2O_3, 99.9% pure) of loba-chemical supplier are taken in stoichiometric proportions. These starting materials were thoroughly mixed with urea (15% weight of the entire mix, 99% pure) in an agate mortar to achieve homogeneity. The entire grounded mix was then sintered to 1200°C for the time of 6 hour and permitted for natural cool up when it reached RT. The resultant product exhibited a frothy texture and was then more grounded to get a homogenous and consistent phosphor material for subsequent characterizations [5].

3.2.2 Characterizations

The phosphors' structural attributes and luminescence optimization were inspected via several characterization techniques. The XRD data recording was accomplished via a D8 Bruker advance X-ray diffractometer within 20° to 80° angle of diffraction with the step of 0.02°/s. To examine the morphological aspects of the Sr_2YNbO_6 sample, a scanning electron microscope (SEM) characterization was utilized. Moreover, the FTIR spectra of the Sr_2YNbO_6:x mol% Eu^{3+} phosphor series were recorded via a Jasco FTIR-4600 spectrometer in transmittance mode, covering the wavenumber range of 400-4000 cm^{-1}. The PL excitation and PL emission spectra of the Sr_2YNbO_6:Eu^{3+} phosphors were monitored at room temperature using a Shimadzu Spectro fluorophotometer. The phosphor series was irradiated with ^{90}Sr beta source to study the TL properties. The thermoluminescence glow curve measurements were done via the Nucleonix TL reader (TL1009) between RT to 250°C, where the heating rate of 2°C/s kept fixed [5].

3.3 Results and Discussion

3.3.1 XRD Studies

The XRD studies of all as-synthesized Sr_2YNbO_6: x mol% Eu^{3+} (x=0-5.0) samples were carried out, and the diffraction patterns are depicted in Figure 3.1 along with the standard ICDD (PDF 04-012-0484) card corresponds to Sr_2YNbO_6 chemical formula. The XRD patterns of all the studied compositions are closely similar. A small variation in the intensity distribution of the diffraction peaks in XRD patterns is mainly due to the addition of Eu^{3+}. All the constituent diffraction peaks of the diffraction pattern were indexed to monoclinic structure with P121/n1 space group and provided enough evidence to validate that the materials are well-synthesized [6,7].

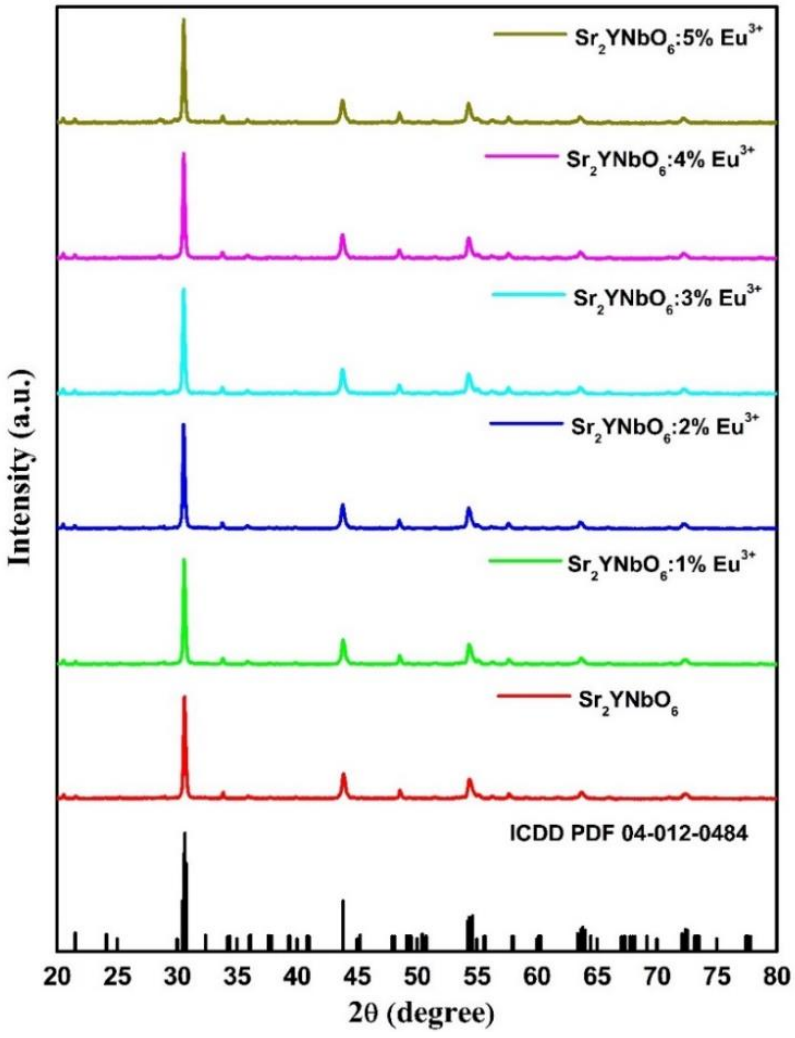

Figure 3.1. XRD of Sr_2YNbO_6: x mol% Eu^{3+} (x= 0-5) phosphors along with standard ICDD reference.

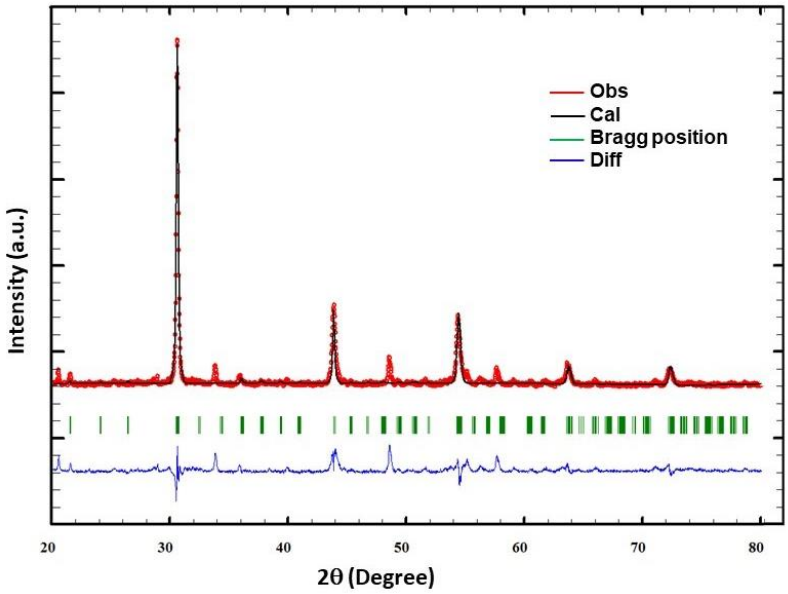

Figure 3.2. Rietveld refined XRD pattern of pure Sr_2YNbO_6 phosphor.

The structural refinement of pure Sr_2YNbO_6 was also carried out in terms of Rietveld refinement and was performed using Fullprof. Suite, a standard computer program to study the diffraction data. Figure 3.2 depicts the Rietveld refined diffraction pattern of the undoped Sr_2YNbO_6 phosphor. The results from the refinement further suggest the monoclinic crystalline structure of the phosphor under study. Overall results from ICDD standard data and Rietveld refinement are significantly correlated. A summary of lattice parameters and structural attributes obtained through the ICDD card and Rietveld refinement are tabulated in Table 3.1. The calculated cell volume of all six samples under study is included. As Eu^{3+} concentration increases, the cell volume marginally increases, as mentioned in Table 3.1.

Samples	**Lattice Parameters**				**χ^2**	**Cell Volume V (Å)**
	a (Å)	**b (Å)**	**c (Å)**	**β**		
Sr_2YNbO_6 (ICDD)	5.81	5.86	8.25	90.20°	-	280.88
Sr_2YNbO_6	5.82	5.84	8.24	90.22°	3.14	280.06
Sr_2YNbO_6:1% Eu^{3+}	5.82	5.86	8.24	90.22°	3.11	281.87
Sr_2YNbO_6:2% Eu^{3+}	5.83	5.86	8.25	90.22°	3.36	282.47
Sr_2YNbO_6:3% Eu^{3+}	5.83	5.86	8.25	90.22°	3.88	282.80
Sr_2YNbO_6:4% Eu^{3+}	5.83	5.86	8.25	90.22°	3.45	282.84
Sr_2YNbO_6:5% Eu^{3+}	5.83	5.86	8.25	90.22°	3.56	282.84

Table 3.1. Summary of lattice parameters obtained through ICDD card and Rietveld refinement.

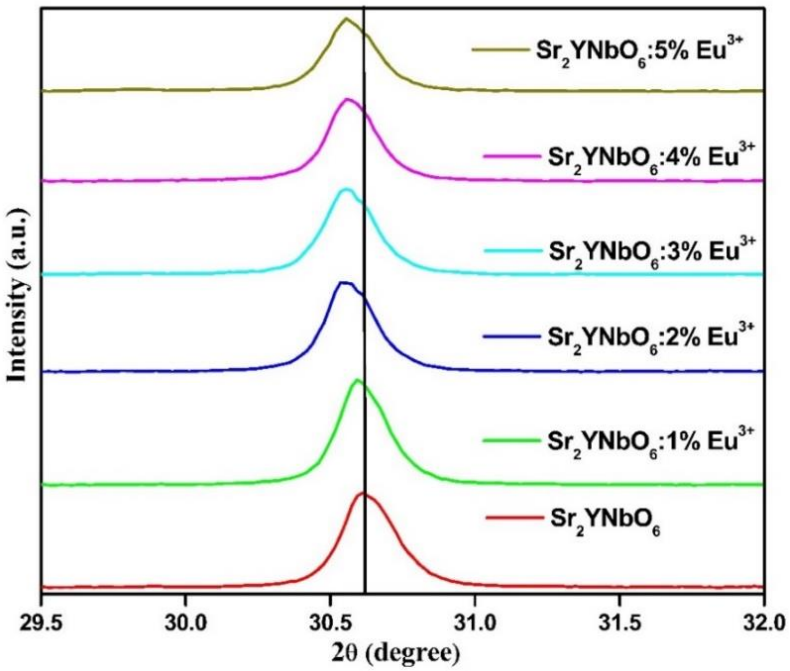

Figure 3.3. Magnified diffraction patterns of undoped and Eu^{3+} doped Sr_2YNbO_6 phosphors.

Figure 3.3 depicts magnified diffraction patterns of the most intense XRD peak among all observed. From the observation of the magnified image, the most intense diffraction peak of doped samples is found to be shifted towards a lower diffraction angle, as shown in Figure 3.3. The gradual shift of 2θ towards a smaller angle is observed as the concentration of Eu^{3+} increases. The observed shift in the position of the diffraction peak was ascribed to Vegard's law. According to Vegard's law, the dopant may not create a separate diffraction peak of its own, instead, it can produce a significant change in the position of the host's peak upon substitution [8]. Due to their similar valence states and closely matched ionic radii, it is highly probable for Eu^{3+} to replace Y^{3+} in the host matrix. The calculation of acceptable percentage difference D_r was utilized to support the previous statement on site substitution [9].

$$D_r = \frac{R_s\,(CN) - R_d\,(CN)}{R_s\,(CN)} \times 100\% \quad \ldots\ldots\ldots\ldots\ldots\ldots\ldots\ldots\ldots\ldots\ldots\ldots\ldots\ldots (3.1)$$

R_s and R_d denote the ionic radius of the replaced ion of the host and the doping ion, respectively. For an ideal substitution of a dopant element in a host lattice, the D_r value would not be more than 30%. In the case of $Sr_2YNbO_6:Eu^{3+}$ phosphor, the calculated value of D_r is obtained to be 4.44%. The computed value of D_r confirms a higher probability of Eu^{3+} ions occupying the Y^{3+} site in the host structure. The shift in diffraction pattern in the direction of lower 2θ further supports

successful substitution of Eu^{3+} ions in place of Y^{3+} ions in the host structure [10]. Furthermore, as the phosphor under instigation crystallized in the perovskite structure, the tolerance factor (T_f) calculation can provide additional confirmation of crystal structure. The tolerance factor was calculated using the formula shown below:

$$T_f = \frac{R_{Sr} + R_O}{\sqrt{2}\left(\frac{R_Y + R_{Nb}}{2} + R_O\right)} \quad \ldots\ldots\ldots\ldots\ldots\ldots\ldots\ldots\ldots\ldots\ldots\ldots\ldots\ldots (3.2)$$

where the notations, R_{Sr}, R_Y, R_{Nb}, and R_O stand for the ionic radius of strontium (Sr), Yttrium (Y), niobium (Nb), and oxygen (O), respectively. The computed value of the tolerance factor is equal to 0.87, giving additional confirmation of the phosphor's monoclinic structure. T_f near to unity suggests cubic perovskite structure.

The crystallite size of the phosphors under study was determined using two different approaches, namely the Debye-Scherer (D-S) formula and the Williamson-Hall (W-H) plot. By analyzing the XRD data, the crystallite size and lattice strain can be calculated using the broadening in the diffraction peak, also called fullwidth at half maximum (FWHM). First, the Debye-Scherer formula for the crystallite size calculation is applied, as given below [11]:

$$D_{hkl} = \frac{K\lambda}{\beta \cos\theta} \quad \ldots\ldots\ldots\ldots\ldots\ldots\ldots\ldots\ldots\ldots\ldots\ldots\ldots\ldots (3.3)$$

where K is the constant, λ stands for the wavelength of X-rays, β stands for the FWHM, and θ denotes diffraction angle. The average size of the crystallites of all the prepared phosphors calculated using the Debye-Scherer formula ranges between 36 nm and 41 nm.

As per W-H plot analysis, the FWHM of the diffraction peak is collectively due to both the crystallite size and lattice strain. The strains (ε) in powders are induced due to lattice distortion and crystal imperfection, and can be calculated using the following formula:

$$\varepsilon = \frac{\beta_{hkl}}{4\tan\theta} \quad \ldots\ldots\ldots\ldots\ldots\ldots\ldots\ldots\ldots\ldots\ldots\ldots\ldots\ldots (3.4)$$

From the Debye-Scherer formula and the above-mentioned strain formula, the derived equation of W-H plot analysis for the calculation of crystallite size is as given below [12]:

$$\beta_{hkl}\cos\theta = \frac{K\lambda}{D} + 4\varepsilon\sin\theta \quad \ldots\ldots\ldots\ldots\ldots\ldots\ldots\ldots\ldots\ldots\ldots\ldots\ldots\ldots (3.5)$$

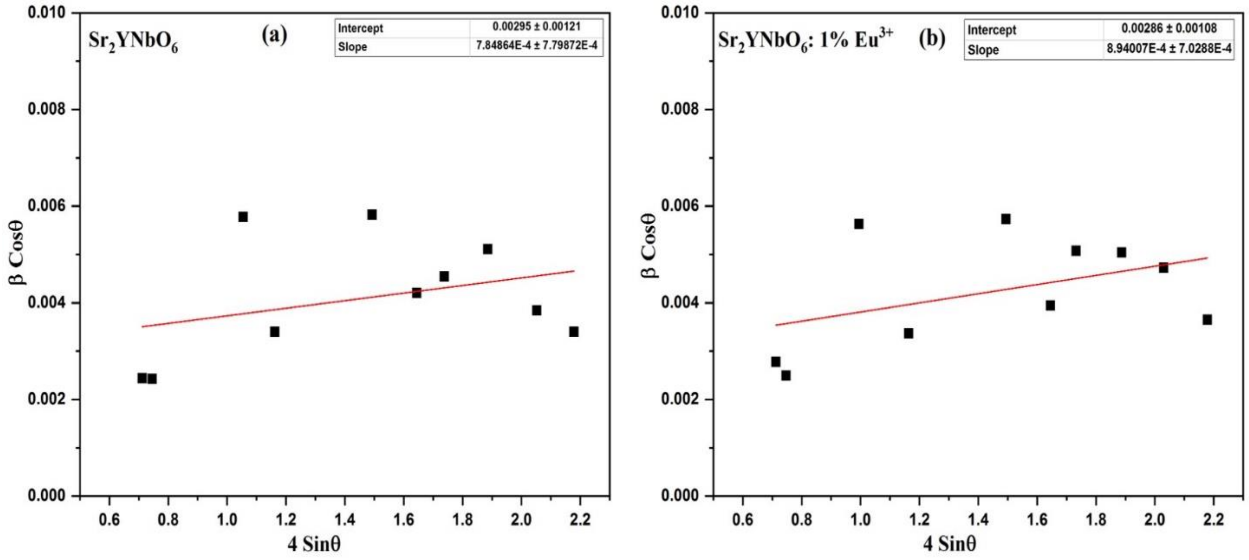

Figure 3.4. W-H plots of Sr_2YNbO_6 (a) and Sr_2YNbO_6:1% Eu^{3+} (b).

Figure 3.4 depicts the W-H plot of pure Sr_2YNbO_6 (a) and 1% Eu^{3+} doped Sr_2YNbO_6 (b) phosphors. In the present case of Sr_2YNbO_6:x mol% Eu^{3+} phosphors, the crystallite size and micro-stain show an increasing trend with rising Eu^{3+} concentration. The parameters computed from both the applied methods are summarized in Table 3.2. The enlargement of crystallites and increasing micro-strain revealed that the higher radius cation Eu^{3+} effectively substitutes smaller radius cation $Y^{3+,}$ which could be reasonably responsible for shifting in the angle of diffraction peaks of the Eu^{3+} doped Sr_2YNbO_6 in comparison with pure Sr_2YNbO_6 sample. Consequently, further modification of crystalline parameters has been observed. The ordered increment in the crystallite size and micro-strain reveals progressively more Y^{3+} ions are replaced by Eu^{3+} ions**.** In comparing Tables 3.1 and 3.2, the cell volume and the crystallite size increase marginally as the concentration of Eu^{3+} increases in host lattice.

Sample		**Pure**	**1mol% Eu^{3+}**	**2mol% Eu^{3+}**	**3mol% Eu^{3+}**	**4mol% Eu^{3+}**	**5mol% Eu^{3+}**
Crystallite size (nm)	**W-H**	49.09	50.63	52.61	55.01	56.75	56.92
	D-S	36.64	39.34	39.17	37.75	39.90	40.33
Strain (ε)		7.84×10^{-4}	8.94×10^{-4}	9.48×10^{-4}	1.49×10^{-3}	1.52×10^{-3}	1.58×10^{-3}

Table 3.2. The crystallite size of Sr_2YNbO_6 phosphors calculated using D-S and W-H methods.

3.3.2 SEM Studies

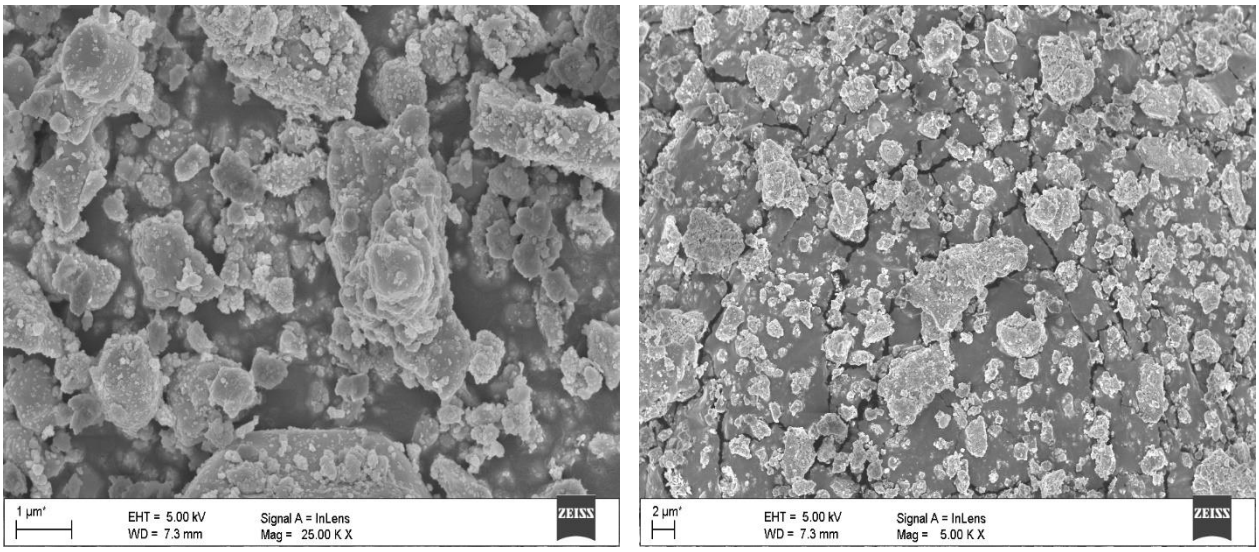

Figure 3.5. SEM micrographs of 4% Eu^{3+} doped Sr_2YNbO_6.

The surface morphology plays an important role and has noticeable effects on the material's properties. To visualize the phosphor particles, the phosphor under investigation was studied through the SEM technique. The SEM micrographs of the Sr_2YNbO_6 sample doped with 4 mol% of Eu^{3+} were captured under different scanning resolutions, and are depicted in Figure 3.5. From the SEM images, a visible agglomeration was observed with non-uniform shapes of the grains with an approximate size between 1 and 2 µm. Whereas, the overall synthesized micro-particles were regularly spread throughout the phosphor. Notably, the SEM micrograph recorded at 1 µm resolution indicates that the average particle size in the sample ranges between 0.5 µm to 2 µm. It is suggested that the mechanical grinding using a ball mill may reduce the size of the particle by less than unity and give uniformly distributed phosphor particles.

3.3.3 FTIR Studies

An investigation of the different modes of vibrations by the atomic bonds forming among the constituent elements was carried out via FTIR study. The functional groups belong to chemical composition can be identified by characterized it via FTIR spectroscopy. Figure 3.6 depicts the FTIR spectra of all studied compositions within 400-2000 cm^{-1}. Using the KBr (Potassium bromide) pellet technique, spectra measurements were accomplished. To make a pallet, first, KBr and phosphor were taken in a 99:1 ratio and ground using mortar and pestle. Later, using dye-set

and pelletizer, the pellets were made by applying pressure of the order of 3 Torr. Subsequently, the measurements were taken using an FTIR spectrometer.

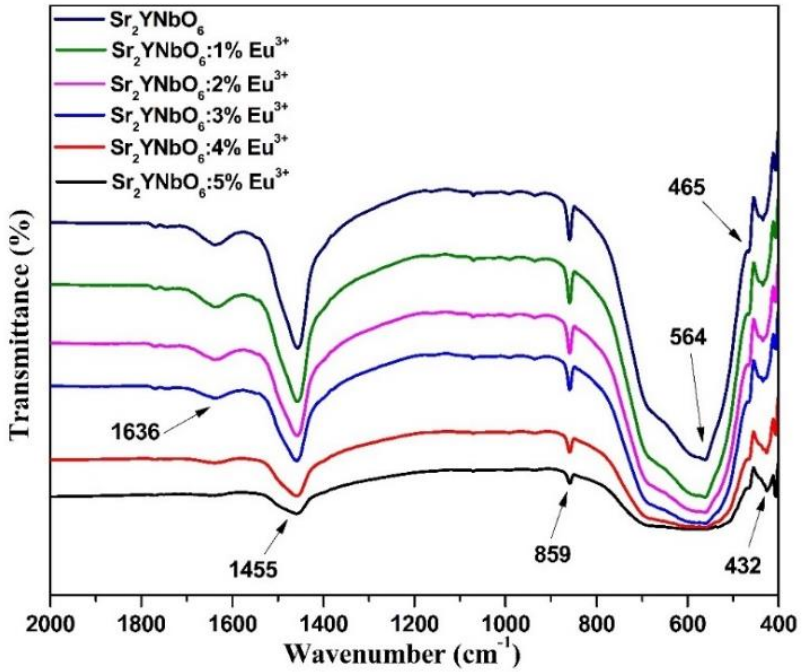

Figure 3.6. FTIR spectrum of Sr_2YNbO_6: x Eu^{3+} (x =0-5 mol%).

The FTIR spectra exhibited well-defined absorption bands representing the existing bonding between the constituent atoms. Among these bands, a band with a spiky nature peaking at around 432 cm^{-1} is attributed to the O-Sr-O bond's bending vibration [13]. Whereas, the typical stretching vibration associated with the yttrium-oxide (Y-O), the metal-oxide bond was observed at around 564 cm^{-1}. A slight hump at about 465 cm^{-1} ascribed stretching vibration corresponds to Y-O metal-oxide bond [14]. In the perovskite type materials, there is a large probability of forming both edge-shared and corner-shared octahedra's. The vibration for corner-shared NbO_6 octahedra mostly lies between the wavenumber range of 750 and 850 cm^{-1}. The edge-shared octahedra of niobates lies within 850-1000 cm^{-1}. The sharp spiky band around 859 cm^{-1} is ascribed to stretching vibrational mode resulting from the formation of edge-connected NbO_6 octahedra. Another broad IR induced band near to 1455 cm^{-1} was attributed to anti-symmetric NbO_6 stretching vibration [15]. Furthermore, the vibrational peak observed 1627 cm^{-1} was attributed to the absorbed moisture (H-OH) during spectra measurements [16].

3.3.4 Photoluminescence Studies

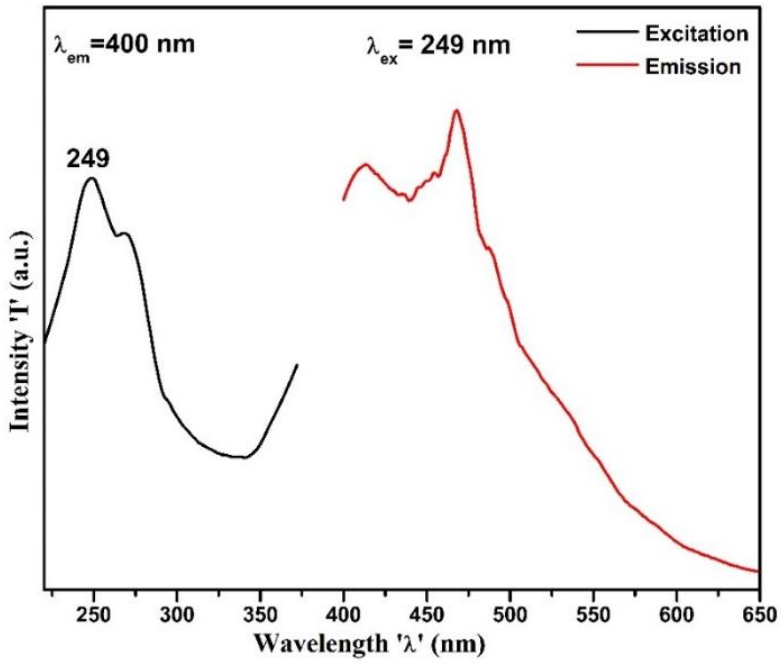

Figure 3.7. Photoluminescence excitation and emission spectra of pure Sr_2YNbO_6.

Figure 3.7 depicts the PL excitation and PL emission spectrum of the base material. From the figure, the excitation band peaking around 249 nm is observed. When the base phosphor is excited at 254 nm, an emission spike is found at 475 nm. The 475 nm peak can be attributed to host emission in the principle of Y^{3+} cation.

Figure 3.8 (a) displays the PL excitation spectrum of Sr_2YNbO_6:1 Eu^{3+} phosphor. The spectrum was recorded at ambient temperature within 220-500 nm. The majority of the excitation spectrum comprises a wide-ranging excitation band centred at 274 nm along with some sharp excitation peaks on the higher wavelength side. When monitored at 614 nm, the following are the most intense excitations observed from 1 mol% Eu^{3+} phosphor, at 274, 396 and 467 nm wavelength. Among which, the highest intensity peak is observed at 396 nm followed by 467 nm and 274 nm. The absorption band peaking at 274 nm is observed due to the charge transfer process. This charge-transfer process occurred between electron reach 2p orbital of O^{2-} and vacant 4f states of Eu^{3+} dopant [17,18]. The other two intense excitations observed at 396 nm and 467 nm are characteristic f-f transitions of Eu^{3+}. The 396 nm excitation is attributed to $^7F_0$-$^5L_6$ transition of Eu^{3+}. However, the excitation peak located at 467 nm is assigned to $^7F_0$-$^5D_2$ transitions of Eu^{3+}, which are characteristic transitions of Eu^{3+} in any host [19-21]. In addition, less intense excitation

peaks observed at 365 nm, 386 nm, and 406 nm are ascribed to $^7F_0$-$^5D_4$, $^7F_0$-$^5L_7$, and $^7F_0$-$^5D_3$ electronic transitions of Eu^{3+}, respectively [22-24].

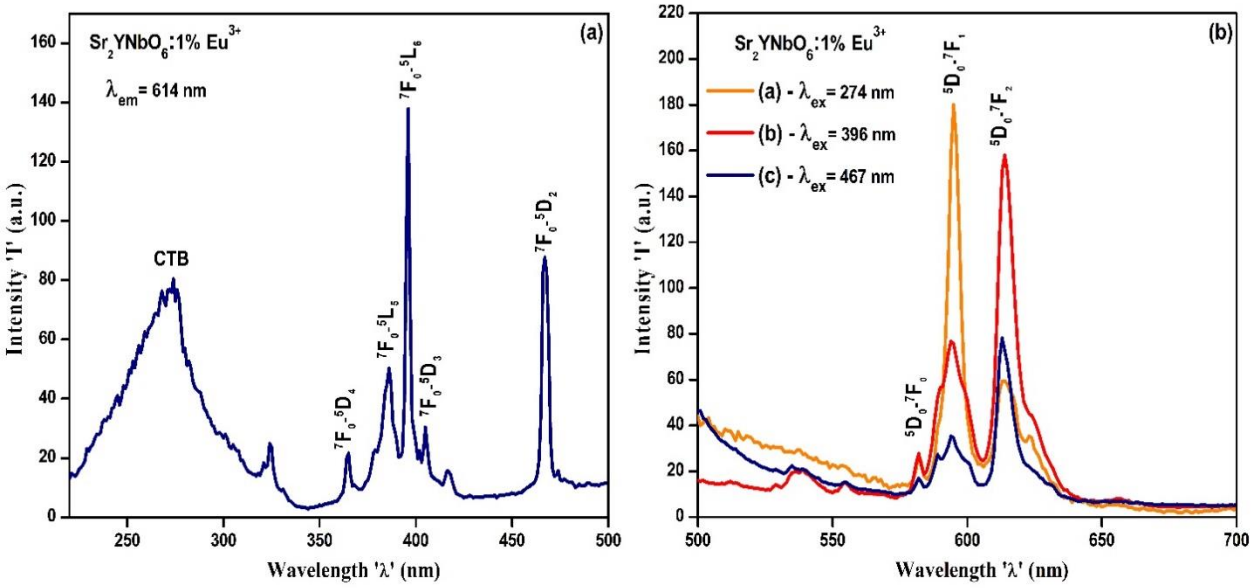

Figure 3.8. PL excitation (a) and PL emission (b) spectra of Sr_2YNbO_6: 1 mol% Eu^{3+} phosphor.

Figure 3.8 (b) depicts the PL emission from 1 mol% Eu^{3+} doped phosphor under study. Curves (a), (b), and (c) are emissions recorded at 274, 396, and 467 nm excitations, respectively. In Curve (a), multiple emission peaks at 582 nm, 596 nm, 612 nm, and 624 nm with various intensities are observed. However, 596 nm peak intensity is very high among all observed. Curve (b) is the emission spectrum Sr_2YNbO_6: 1 mol% Eu^{3+} phosphor recorded with 396 nm. Three intense emission peaks at 582 nm, 596 nm, and 614 nm are observed, among which the peak at 614 nm was the intense one when compared to other observed peaks. The 614 nm emission peak is observed due to a hypersensitive electric dipole (ED) transition when excited at 396 nm. Curve (c) is the emission of the phosphor when excited with 467 nm. Under 467 nm excitation, emissions at 582 nm, 596 nm and 614 nm are observed, in which the emission at 614 nm was intense one. In curve (c), the intensity of the emission peak at 614 nm is nearly half when compared to the intensity obtained with 396 nm excitation.

Under 274 nm excitation, a strong orange-red spectral emission corresponding to electronic transition occurring within the 4f level of europium ions was observed. A prominent emission transition observed at 596 nm is ascribed to the magnetic-dipole (MD) transition of Eu^{3+} occurring between $^5D_0$ and $^7F_1$. The emission peak with lesser intensity at 582 nm was attributed to the

electric dipole (ED) transition from $^5D_0$-$^7F_0$. Moreover, a group of emission peaks within 610-625 nm were ascribed to electric dipole (ED) transitions taking place from $^5D_0$-$^7F_2$ states of Eu^{3+} [25-27]. Upon 396 nm, a near UV excitation, and 467 nm, a blue-LED excitation, a dominant down-conversion red spectral emission resulting due to the hypersensitive ED transition $^5D_0$-$^7F_2$ of Eu^{3+} ions are observed [28-30]. A closely identical emission patterns were produced upon both applied excitations. A relatively less intense emission peaks observed at 582 nm and 596 nm are ascribed to ED transition $^5D_0$-$^7F_0$ and MD transition $^5D_0$-$^7F_1$ of Eu^{3+}, respectively. Table 3.3 summarized the excitation and emission intensity counts of 1 mol% Eu^{3+} doped Sr_2YNbO_6 phosphor.

Ex Peak	**274 (nm) (E= 4.52 eV)**		**396 (nm) (E= 3.13 eV)**		**467 (nm) (E= 2.65 eV)**	
Ex Intensity	80		138		87	
	Emission Peak (nm)	**Emission Intensity**	**Emission Peak (nm)**	**Emission Intensity**	**Emission Peak (nm)**	**Emission Intensity**
Emission	582	27	582	28	582	17
	596	180	596	77	596	35
	614	60	614	158	614	78

Table 3.3. PL intensities of various excitation and emission peaks of 1 mol% Eu^{3+} activated Sr_2YNbO_6 phosphor.

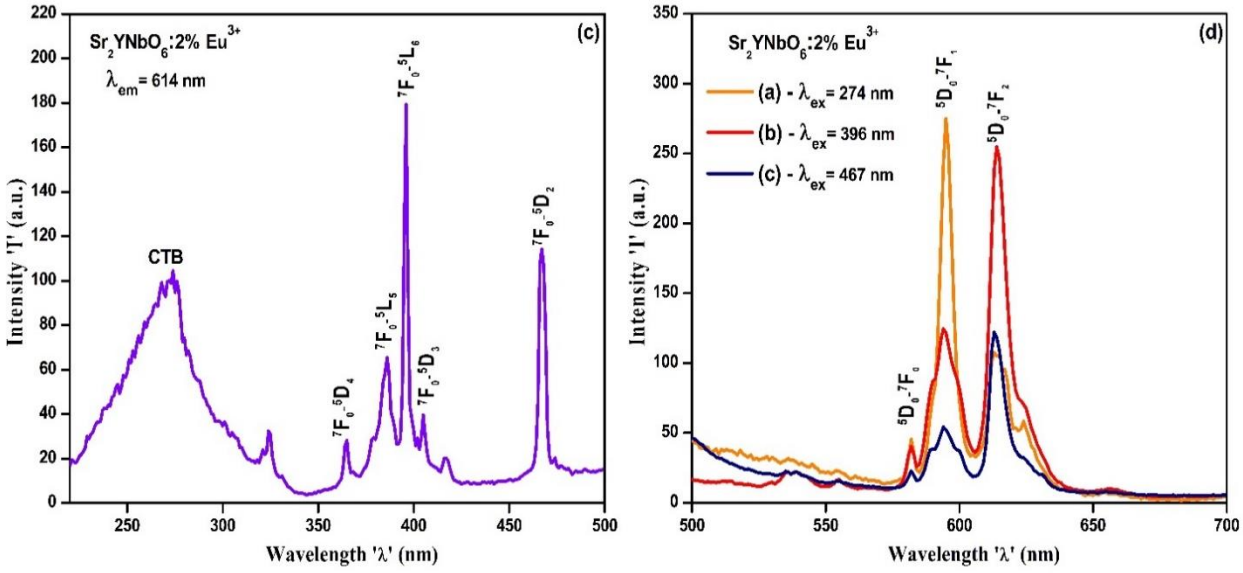

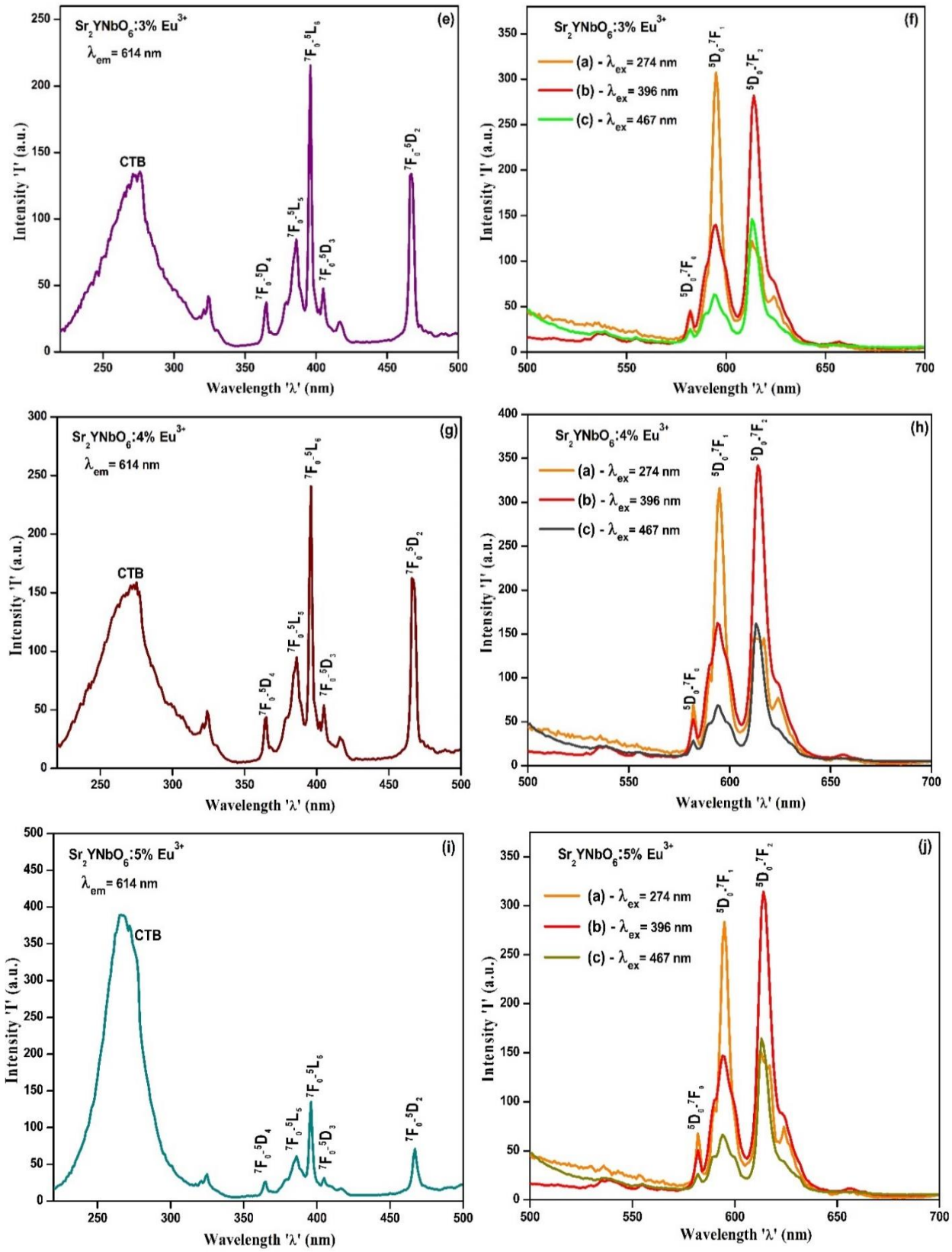

Figure 3.8. (c-j) PL excitation and respective PL emission spectra of 2 mol% to 5 mol% Eu^{3+} activated Sr_2YNbO_6 phosphors.

Ex Peak	**274 (nm) (E= 4.52 eV)**		**396 (nm) (E= 3.13 eV)**		**467 (nm) (E= 2.65 eV)**	
Ex Intensity	104		180		114	
	Emission Peak (nm)	**Emission Intensity**	**Emission Peak (nm)**	**Emission Intensity**	**Emission Peak (nm)**	**Emission Intensity**
Emission	582	45	582	40	582	22
	596	275	596	124	596	54
	614	108	614	254	614	122

Table 3.4. PL intensities of various excitation and emission peaks of 2 mol% Eu^{3+} doped Sr_2YNbO_6 phosphor.

Ex peak	**274 (nm) (E= 4.52 eV)**		**396 (nm) (E= 3.13 eV)**		**467 (nm) (E= 2.65 eV)**	
Ex intensity	133		215		133	
	Emission peak (nm)	**Emission intensity**	**Emission peak (nm)**	**Emission intensity**	**Emission peak (nm)**	**Emission intensity**
Emission	582	45	582	45	582	25
	596	307	596	140	596	63
	614	122	614	282	614	145

Table 3.5. PL intensities of various excitation and emission peaks of 3 mol% Eu^{3+} doped Sr_2YNbO_6 phosphor.

Ex Peak	**274 (nm) (E= 4.52 eV)**		**396 (nm) (E= 3.13 eV)**		**467 (nm) (E= 2.65 eV)**	
Ex Intensity	158		240		163	
	Emission Peak (nm)	**Emission Intensity**	**Emission Peak (nm)**	**Emission Intensity**	**Emission Peak (nm)**	**Emission Intensity**
Emission	582	70	582	53	582	28
	596	316	596	162	596	69
	614	144	614	341	614	161

Table 3.6. PL intensities of various excitation and emission peaks of 4 mol% Eu^{3+} doped Sr_2YNbO_6 phosphor.

Ex Peak	274 (nm) (E= 4.52 eV)		396 (nm) (E= 3.13 eV)		467 (nm) (E= 2.65 eV)	
Ex Intensity	350		134		71	
	Emission Peak (nm)	Emission Intensity	Emission Peak (nm)	Emission Intensity	Emission Peak (nm)	Emission Intensity
Emission	582	68	582	50	582	26
	596	283	596	146	596	66
	614	150	614	314	614	164

Table 3.7. PL intensities of various excitation and emission peaks of 5 mol% Eu^{3+} doped Sr_2YNbO_6 phosphor.

Figure 3.8 (c-j) depicts the PL excitation and their corresponding PL spectra of the Sr_2YNbO_6:x mol% Eu^{3+} (x=2, 3, 4, and 5) phosphors. All the phosphors with various europium concentrations displayed a similar pattern of PL excitation and PL emission, in which the phosphor doped with 4 mol% of Eu^{3+} displays maximum PL intensity. Interestingly, the absorption due to the charge transfer process in 5 mol% Eu^{3+} doped phosphor was found to be very intense when compared to Eu^{3+}'s f-f transitions. Table 3.4-3.7 summarized the excitation and emission intensity counts of 2-5 mol% Eu^{3+} doped Sr_2YNbO_6 phosphors. Upon close examination of the PL results obtained from all Eu^{3+} doped Sr_2YNbO_6 double perovskite, it is concluded that, all the doped phosphors under investigation produce similar PL excitations and emissions in which the intensities were changing upon varying doping concentrations.

Figure 3.9; 3.10 (a), (b), and (c) are the combined graphs of PL excitation and subsequent emission of Eu^{3+} doped phosphors under study. From Figure 3.9, 3.10 (a-c), and from Tables 3.3, 3.4, 3.5, 3.6, and 3.7, it is found, when the phosphor is excited with 274, 396, and 467 nm excitations, the highest PL peak intensity of the obtained peaks are observed upon 4 mol% Eu^{3+} doping. All the observed peaks in the present phosphor system are standard europium (III) emissions.

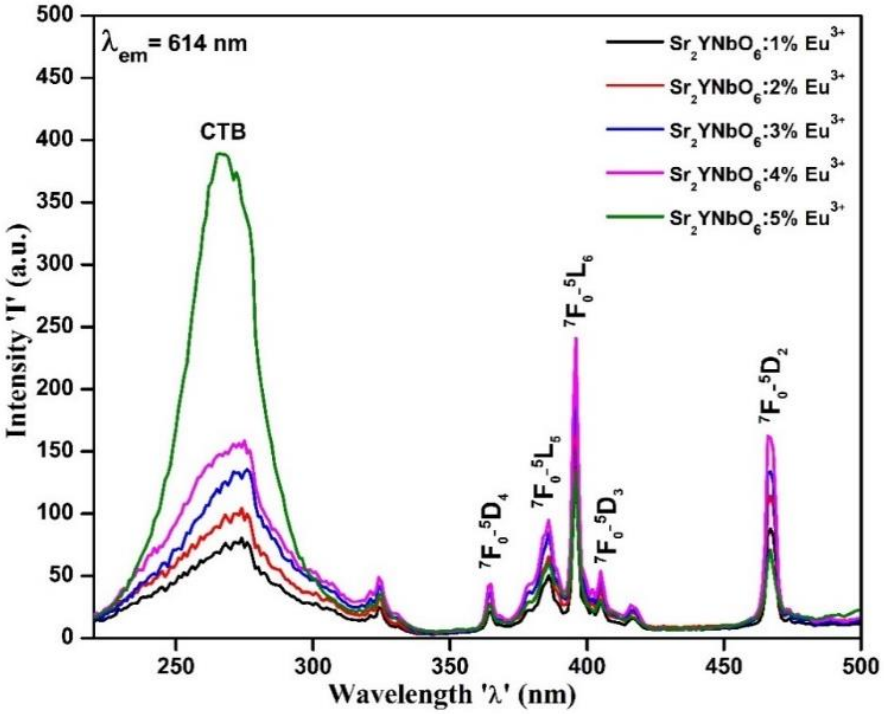

Figure 3.9. Photoluminescence excitation spectra of Sr_2YNbO_6: x mol% Eu^{3+} (x =1-5) phosphors.

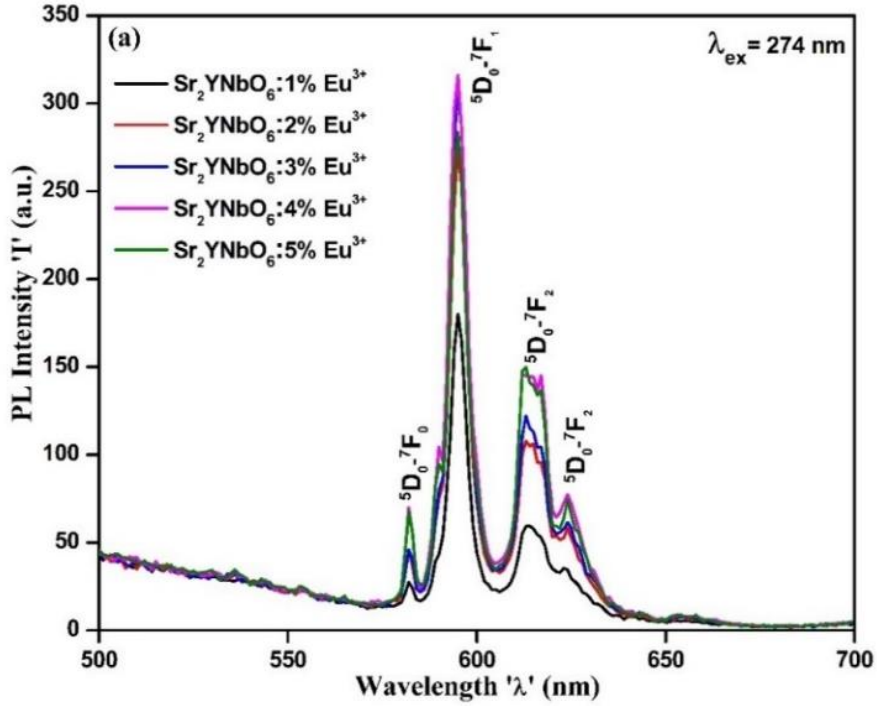

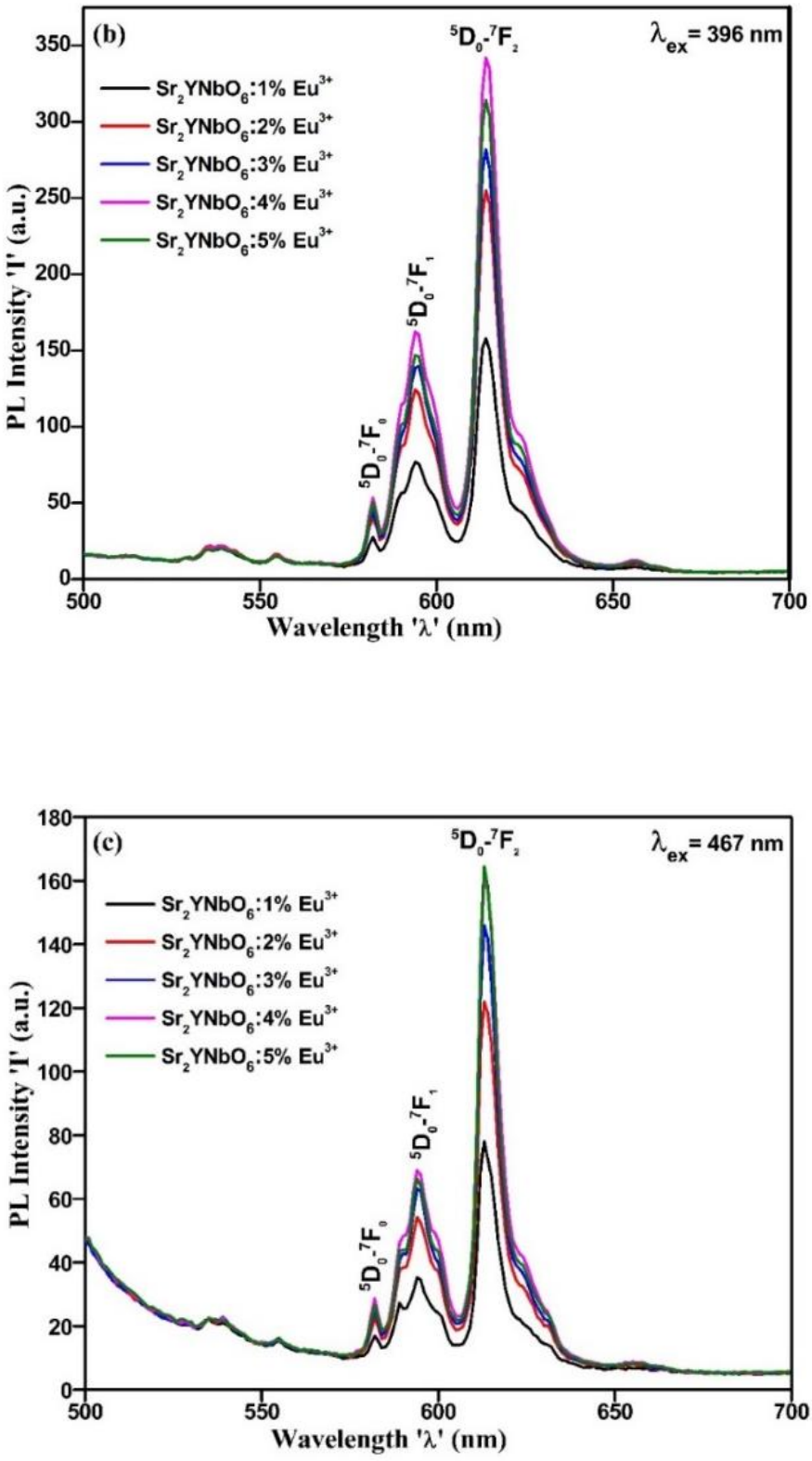

Figure 3.10. PL emission spectra of Sr_2YNbO_6: x mol% Eu^{3+} (x =1-5) recorded under (a) 274 nm, (b) 396 nm, and (c) 467 nm excitation wavelengths.

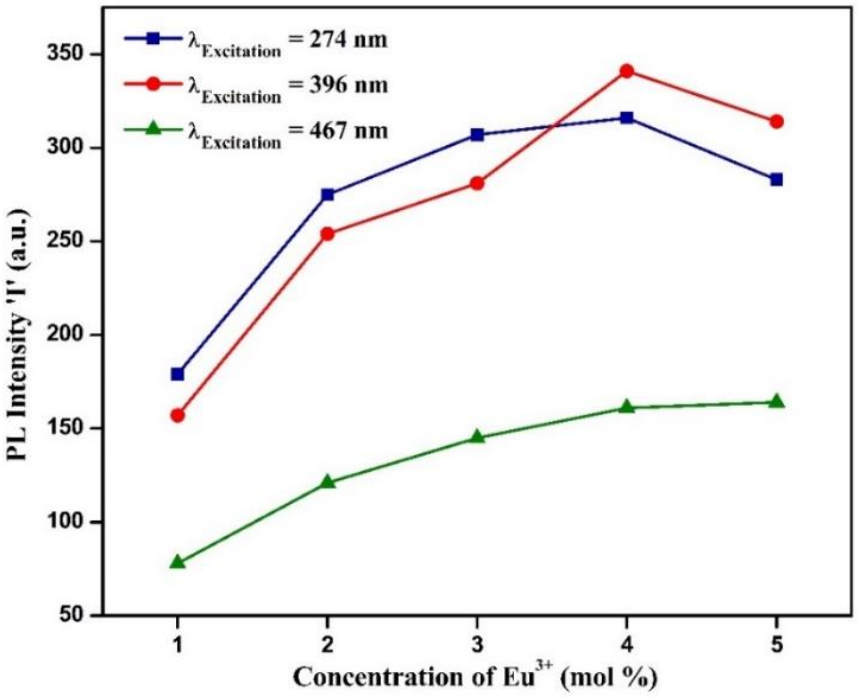

Figure 3.11. Plot of PL intensity vs. doping concentration.

Figure 3.11 shows the observed PL peak intensities for different excitations versus Eu^{3+} doping concentration in molar %. As the doping level of Eu^{3+} was increased, there was a consistent increase in the intensity of PL emission within the red spectral region. The intensity of PL emission becomes highest when the phosphor contains 4 mol% of Eu^{3+}. When 5 mol% Eu^{3+} was introduced into the host material, a phenomenon of concentration quenching arose. Upon 5 mol% Eu^{3+} doping a reduction of PL intensity of around 10% is observed for all the emissions excited at 274 nm and 396 nm, excitations. However, in the case of 467 nm excitation, the PL intensity met saturation upon reaching a 4 mol% Eu^{3+} concentration.

The phenomenon of intensity quenching involved nonradiative exciton relaxation, as the activator concentration reached a specific concentration. This non-radiative energy transfer between the host lattice and the active center resulted either by multipolar interactions or exchange interactions. Verification of this interaction was done via the calculation of the critical distance (R_c) [31];

$$R_c = 2\left(\frac{3V}{4\pi X_c N}\right)^{1/3} \quad \ldots\ldots\ldots\ldots\ldots\ldots\ldots\ldots\ldots\ldots\ldots\ldots\ldots\ldots (3.6)$$

where V denotes unit cell volume, X_c denotes the critical doping level, and N denotes host cation numbers within the unit cell. Herein, the computed value of R_c equals to 18.8 Å, indicating that the multipolar interaction is mainly responsible for the intensity quenching.

Under the excitation wavelength of 274 nm corresponding to the charge transfer state, the photoluminescence emission displays highest intensity of MD ($^5D_0$-$^7F_1$) transition when compared to ED ($^5D_0$-$^7F_2$) transition. This phenomenon arises in the case of CTB excitation, because the red spectral emission resulting from ED transition was then suppressed by the MD transition of Eu^{3+}. In contrast, under 396 nm excitation, the PL intensity due to allowable MD transition appears less intense compared to the intensity of the allowed ED transition. This observation directs toward the substitution of doping ions Eu^{3+} in a non-inversion symmetry site within the base matrix. If the MD transition produces greater intensity than the ED transition, it would suggest the presence of Eu^{3+} ions occupying an inversion center. However, a higher intensity from the ED transition than the MD transition indicates the occupancy of Eu^{3+} ions without symmetric inversion center. To determine the symmetric site occupancy of Eu^{3+} within the host matrix, the calculation of an asymmetry ratio, denoted as the integral intensity ratio "R" useful. This ratio is expressed as $R = I(5D0 - 7F2) / I(5D0 - 7F1)$, where I($^5D_0$-$^7F_2$) indicates maximum intensity counts of the ED transition and I($^5D_0$-$^7F_1$) denotes the maximum intensity counts of the MD transition. The determined R value appears remarkably high, falling within the range of 2 to 2.5, which is very much greater than unity provided solid confirmation of the occupancy of Eu^{3+} at non-inversion sites within the host matrix [32]. The PL emission recorded with 467 nm excitation looks relatively less intense when compared to the PL emission recorded with 396 nm excitation. This difference in intensities is attributed to the increased absorption of incident photons due to the $^7F_0$-$^5L_6$ transition when compared with $^7F_0$-$^5D_2$ transition.

The thermal stability of the luminescent material plays a significant role in the selection of phosphor to be used in device application in principle of LED application. The thermal stability of the phosphor material for device application should be comparable with the operating temperature of the LED. A study on thermal stability signifies the capability of phosphor to be incorporated in pc-LED devices, and in high-power lighting displays [33,34]. Temperature factor significantly affects the luminescence performance of phosphors and can lead to variations in the color rendering index and reduction in PL intensity. To examine the performance of the phosphor under

study towards higher temperature conditions, a temperature dependent PL spectrum of most luminous phosphor among all studied is recorded.

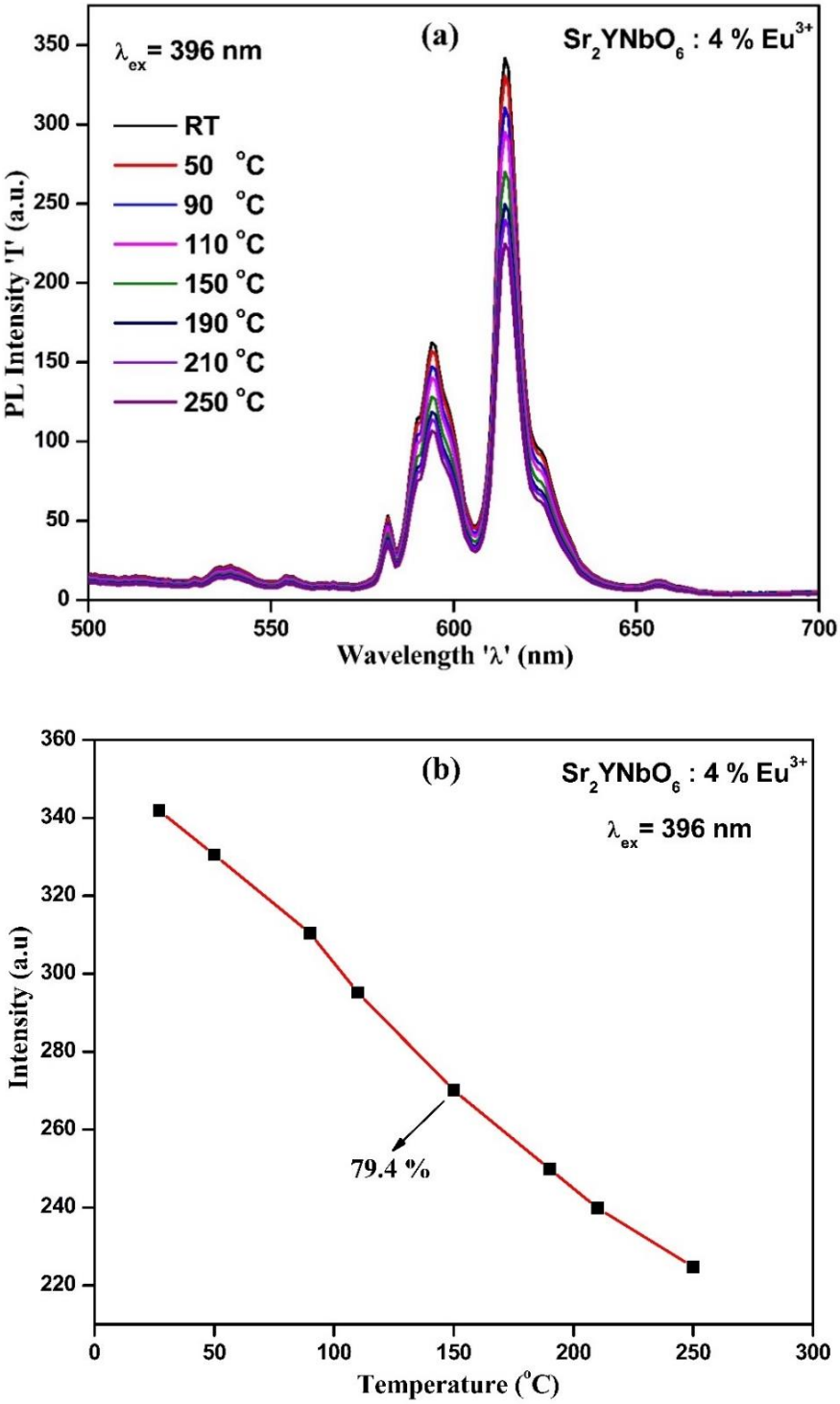

Figure 3.12. PL emission spectra of Sr_2YNbO_6: 4 mol% Eu^{3+} at different temperatures (a); plot of PL intensity vs. Temperature (b).

Figure 3.12 (a) demonstrates the relation between PL emission intensity and temperature from 4 mol% Eu^{3+} activated Sr_2YNbO_6 phosphor when excited with 396 nm. The measurements were taken from RT to 250 °C. From the Figure, it is found that the PL intensity is linearly decreases with rising temperature and remained 79.4 % at 150 °C in comparison with PL intensity recorded at RT. Figure 3.12 (b), denotes the relationship between PL intensity and temperature. The decrease in PL growth with rising temperature implies to thermal quenching phenomenon [35]. Except reduced PL intensity counts, the position of emission peak and the nature of spectrum remained unaffected with increasing temperature. The Eu^{3+} doped perovskite sample under study exhibits a remarkably less thermal quenching behavior, with intensity of PL remaining 79.4 % at 150 °C temperature in contrast with its intensity obtained at 27 °C. The extraordinary thermal stability may be due to the rigid perovskite structure of the phosphor, which can effectively reduce the thermal quenching even after increasing the LED operating temperature [36]. Several approaches, such as multi-phonon relaxation, thermally activated photoionization, and thermally activated crossing caused at the higher energy state to the ground state, are take part in the thermal quenching phenomenon [37].

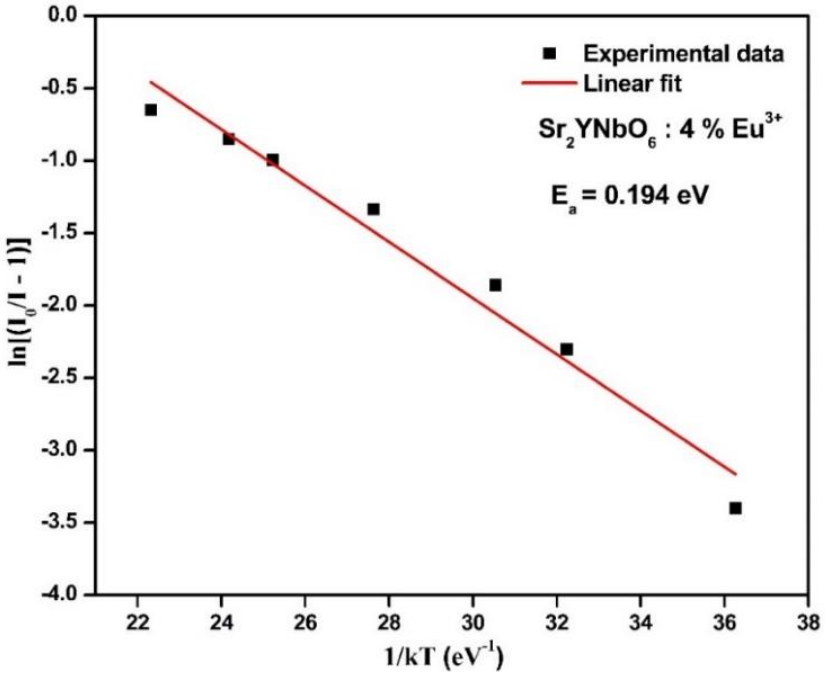

Figure 3.13. Plot of ln[(I_0/I)-1] vs.1/kT.

In addition to the thermal stability of phosphor, the activation energy can also be determined by utilizing temperature dependent PL spectra. Figure 3.13 depicts the plot between

ln[(I_0/I)-1] and 1/kT for Sr_2YNbO_6: 4% Eu^{3+} phosphor, and was drawn from the values of temperature dependent PL. By using the Arrhenius model, the activation energy of the Sr_2YNbO_6:4 mol% Eu^{3+} sample of the thermal quenching was estimated via the following formula [38]:

$$I(T) = \frac{I_0}{1 + c\ \exp\ (-E_a/kT)} \dots\dots\dots\dots\dots\dots\dots\dots\dots\dots\dots (3.7)$$

I(T) denote the intensity of PL at various temperatures, I_0 denotes intensity of PL emission at room temperature. E_a stands for activation energy, k denotes the Boltzmann constant, whereas c is the constant. From the slope of ln[(I_0/I)-1] vs.1/kT, the E_a of the phosphor under study was determined to be 0.194 eV. The obtained activation energy from the thermal quenching study found quite good, suggesting excellent thermal stability of the phosphor. This reasonably high E_a confirms the high thermal stability of the as-prepared perovskite phosphors [39].

As shown in the emission spectra of all the phosphors under study at different excitation wavelengths, a strong red spectral emission at 614 nm is observed, which is result due to the $^5D_0$-$^7F_2$ hypersensitive ED transition. The study on PL decay provides an essential information regarding relaxation dynamics in the phosphor's excited state. A multi-phonon relaxation, radiative decay, and non-radiative ion-ion interaction are be the cause of the relaxation dynamics.

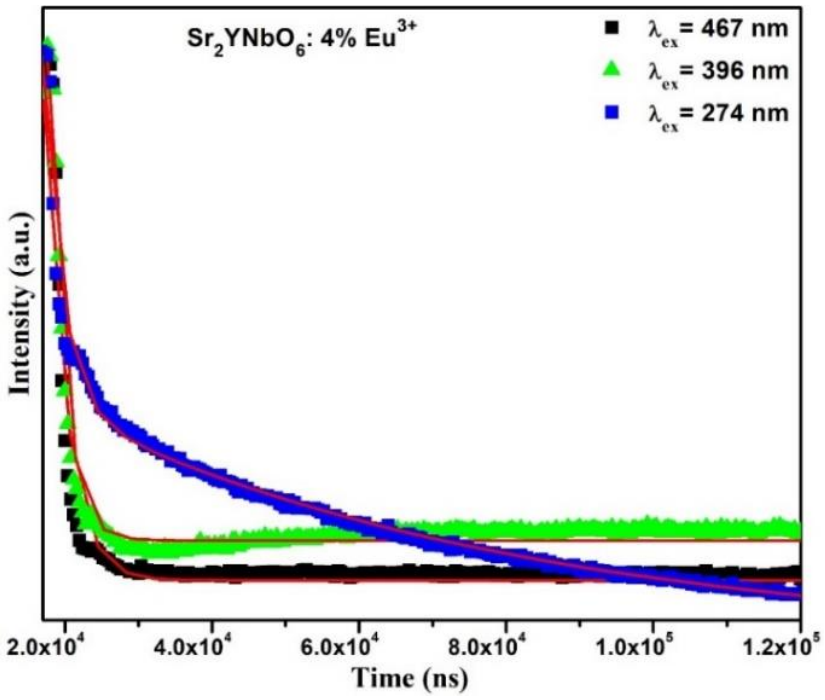

Figure 3.14. PL decay lifetime curves of Sr_2YNbO_6: 4% Eu^{3+}.

Herein, the influence of different excitations on PL emission decay was investigated. Figure 3.14 displays the measured decay curves for the 614 nm emission wavelength and for all three mentioned excitations. The lifetime decay curve corresponds to charge transfer state with center wavelength of 274 nm was fitted over double exponential curve.

$$I = I_o + A_1 \exp\left(-\frac{t}{\tau_1}\right) + A_2 \exp\left(-\frac{t}{\tau_2}\right) \quad \text{..... (3.8)}$$

here, τ_1 and τ_2 represents decay constants, where τ_1 indicates fast decay, whereas τ_2 stands for the slow decay. A_1 and A_2 are the constants. To calculate the average decay (τ) in case of the double exponential function, following equation of average decay time was utilized,

$$\tau = (A_1\tau_1^2 + A_2\tau_2^2)/(A_1\tau_1 + A_2\tau_2) \quad \text{..... (3.9)}$$

However, the single exponential function was taken into the account to fit the decay curves correspond to 396 and 467 nm excitations, and can presented by following equation [40,41];

$$I = I_o + A \exp\left(-\frac{t}{\tau}\right) \quad \text{.....(3.10)}$$

where all the identities have its usual meanings. The computed decay lifetime for excitation wavelength of 274 nm is 1.298 μs, for 396 nm is 1.957 μs, and for 467 nm is 2.618 μs. The reduction in PL emission, which may occur because of cross-relaxation, causes the decay lifetime to decrease fast.

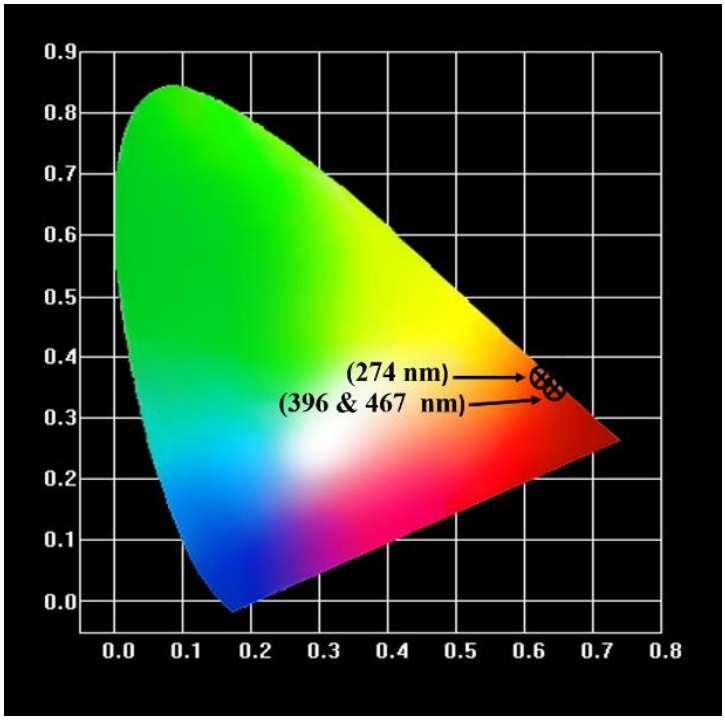

Figure 3.15. CIE diagram of Sr_2YNbO_6:4 mol% Eu^{3+}.

The CIE color coordinates refer to a system of specifying colors as defined by the International Commission on Illumination (CIE). The CIE color points are a three-dimensional model that provides a standardized way to describe the colors. To verify the color performance and color purity of the phosphor, the CIE color coordinates of all the phosphors under investigation were computed. The findings of the color coordinates of 4 mol% Eu^{3+} activated Sr_2YNbO_6 phosphor are depicted in Figure 3.15. The computed CIE coordinates of the 4 mol% Eu^{3+} doped Sr_2YNbO_6 sample are (0.534, 0.449) for the excitation of 274 nm, (0.587, 0.405) for the excitation of 396 nm and (0.517, 0.457) for 467 nm excitation. From the diagram, it is observed that the CIE points obtained for 274 nm excitation lie in the orange-red spectral region; however, the color coordinates obtained for 396 nm, and 467 nm lie in the pure red spectral region [42,43]. In addition, the following formula was used to calculate the color purity of all the Sr_2YNbO_6 phosphors under study:

$$\text{Color Purity} = \frac{\sqrt{(x-x_s)^2+(y-y_s)^2}}{\sqrt{(x_d-x_s)^2+(y_d-y_s)^2}} \quad \ldots\ldots\ldots\ldots\ldots\ldots\ldots\ldots\ldots\ldots \quad (3.11)$$

where x and y_s stand for the CIE points of the sample; x_s and y_s stands for the 1931 CIE Standard Source illuminant white point; and, x_d and y_d for the CIE color coordinates of pure red color, respectively. Under various excitations, the obtained values of color purity of Sr_2YNbO_6:Eu^{3+} phosphors found very good, indicating that the Eu^{3+} doped Sr_2YNbO_6 double perovskite is a good phosphor for its application in WLEDs.

Furthermore, to estimate the color quality of PL emissions, the approach of color correlated temperature (CCT) was extensively applied. The CCT for the all studied phosphor compositions was calculated via the McCamy method using the CIE color coordinates. The following formula was utilized for CCT calculation [44]:

$$CCT = -449\,n^3 + 3525\,n^2 - 6823.3\,n + 5520.33 \quad \ldots\ldots\ldots\ldots\ldots\ldots \quad (3.12)$$

Where, n stands for $\frac{x-x_e}{y-y_e}$ (x_e=0.3320, y_e=0.1858). The CIE points of all the phosphors under study at different excitation wavelengths, along with CCT were tabulated in Table 3.8.

From the overall PL studies, temperature dependent PL studies, PL decay studies, CIE studies and CCT studies, it is concluded that the 4 mol% Eu^{3+} doped Sr_2YNbO_6 phosphor is a as good red-component for its application in UV (396 nm) excited WLEDs.

Sample	Excitation Wavelength	CIE co-ordinates		Color purity (%)	CCT (K)
		X	Y		
Sr_2YNbO_6:1 % Eu^{3+}	274 nm	0.478	0.495	80.80	3032.09
	396 nm	0.558	0.430	74.34	1904.71
	467 nm	0.457	0.505	65.55	3355.75
Sr_2YNbO_6:2 % Eu^{3+}	274 nm	0.517	0.463	83.57	2411.59
	396 nm	0.581	0.410	78.13	1739.82
	467 nm	0.496	0.474	66.81	2696.75
Sr_2YNbO_6:3 % Eu^{3+}	274 nm	0.524	0.457	84.36	2306.81
	396 nm	0.587	0.405	79.25	1719.9
	467 nm	0.508	0.465	67.84	2510.83
Sr_2YNbO_6:4 % Eu^{3+}	274 nm	0.534	0.449	85.76	2174.81
	396 nm	0.595	0.398	80.78	1713.03
	467 nm	0.517	0.457	68.57	2374.89
Sr_2YNbO_6:5 % Eu^{3+}	274 nm	0.527	0.455	84.83	2266.33
	396 nm	0.591	0.401	79.97	1713.79
	467 nm	0.513	0.461	68.30	2442.02

Table 3.8. CIE color coordinates determined parameters.

3.3.5 Thermoluminescence Studies

Thermoluminescence (TL) is a physical phenomenon and a technique used in various scientific fields, mainly in archaeology, geology, and materials science. The TL is an exciting phenomenon of light emission from the materials like semiconductors and insulators after high energy radiation exposure upon controlled heating. The thermoluminescence dosimetry (TLD) is established technique to measure very low to very high absorbed radiation, such as alpha rays, beta rays, gamma rays, UV rays and X-rays [45]. Herein, author of the thesis is primarily focusing on the TL characterization of the niobate based double perovskites. The aim is to study the TL growth (intensity) with increasing high energy beta radiation dose from ^{90}Sr beta source. To accomplish the targeted aim, the prepared phosphors were subjected for TL studies. By measuring the intensity of the emitted light, the amount of ionizing radiation that the material has been exposed can be estimated.

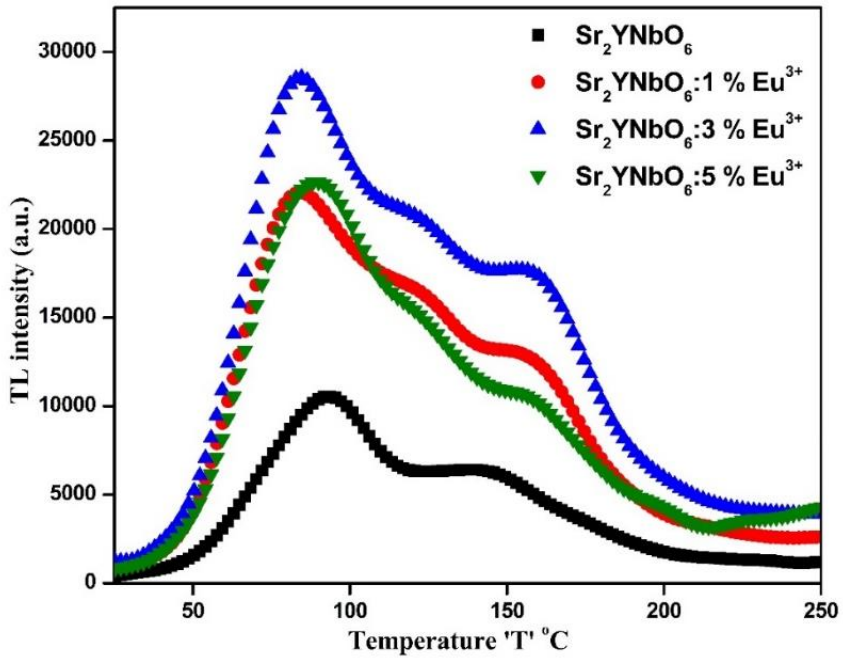

Figure 3.16. Thermoluminescence glow curves of Sr_2YNbO_6:x mol% Eu^{3+} (x=0, 1, 3, 5).

To examine the TL behaviour of the phosphors under study, they all are exposed to various beta doses. Every time 3 mg beta irradiated powder phosphor is taken for TL measurements, and glow curves were recorded from RT to 250 °C with a 2 °C/s heating rate. Upon beta exposure, the phosphors under investigation shows an excellent TL response.

Figure 3.16 displays the TL glow curves of pure; 1 mol%, 3 mol%, and 5 mol% Eu^{3+} containing Sr_2YNbO_6 phosphors after being irradiated with a 10 Gy dose of beta rays. The most intense TL peaks of all the phosphor compositions were appeared at approximately 83 °C followed by lesser intense TL glow peaks towards the higher temperature side. From the figure, a very good intense TL peak is found for the undoped sample. For all the phosphor under investigation, a relatively good intense TL peak is found at around 85 °C and a hump at 150 °C. It should be noted, as Eu^{3+} concentration increases, one more peak at around 117 °C is observed. Furthermore, the peak observed at 150 °C in the undoped sample is found to be shifted to around 170 °C in all three 1 mol%, 3 mol% and 5 mol% doped samples. It is also noted from the acquired TL glow curves, as the Eu^{3+} concentration increases in phosphor under study, the TL intensity of all the observed peaks increases up to 3 mol% of doping, and then decreases by 15 % for 5 mol% of Eu^{3+} doping [46-48]. With doping of Eu^{3+}, the intensity of TL glow peaks gets enhanced, as the defect centres were created more upon doping. The TL glow curves showed the highest glow at a concentration

of 3 mol% of Eu^{3+}, as shown in Figure 3.17. The concentration quenching was observed when the Eu^{3+} doping level raised from 3 mol% to 5 mol%. This quenching in TL glow is attributed to a reduction in the separation between successive dopant ions. Increasing the doping level ensuing perturbation in the dopant's energy levels and was then resulting in TL intensity quenching [5].

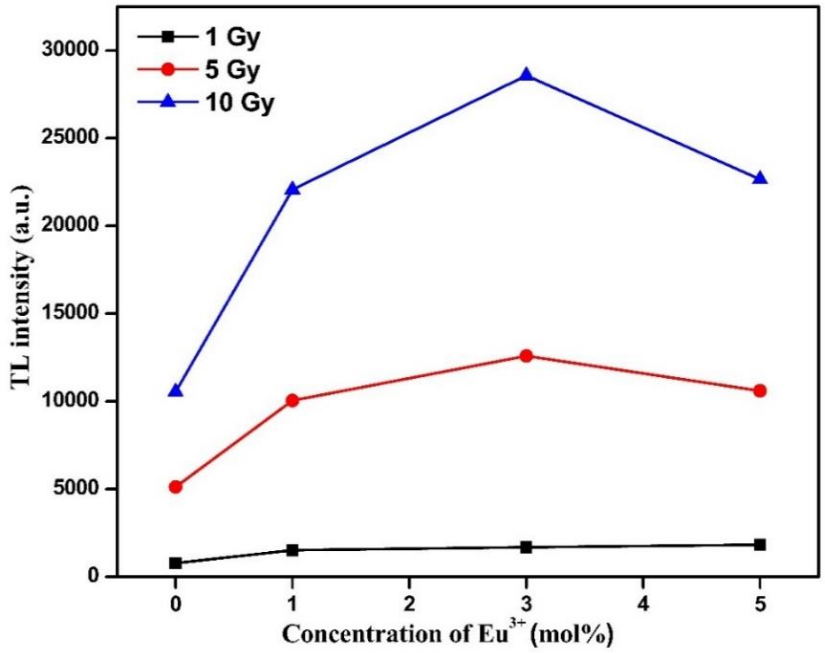

Figure 3.17. TL intensity response to different Eu^{3+} concentrations.

In another experiment, the TL glow curves of all four mentioned phosphors were recorded after 1, 5, and 10 Gy beta doses in order to study the dose response. The TL dose response of the phosphor can be studied by the relation between TL intensity counts and the amount of ionizing radiation it has been exposed to. This relationship follows certain patterns and principles. In the initial range of ionizing radiation doses, the TL response of a material may linear. This means that the emitted thermoluminescent signal is directly related to the absorbed dose of ionizing radiation. The linear relationship of dose with TL intensity is particularly useful for determining doses in circumstances where the radiation exposure is relatively low. However, as the radiation dose reaches the threshold value, the TL response of the material can approach a saturation point. This means that the emitted thermoluminescent signal may reach a maximum value beyond which further increases in dose do not lead to proportional increases in the TL signal. Saturation can occur due to the filling of available trapping sites for electrons within the crystal lattice.

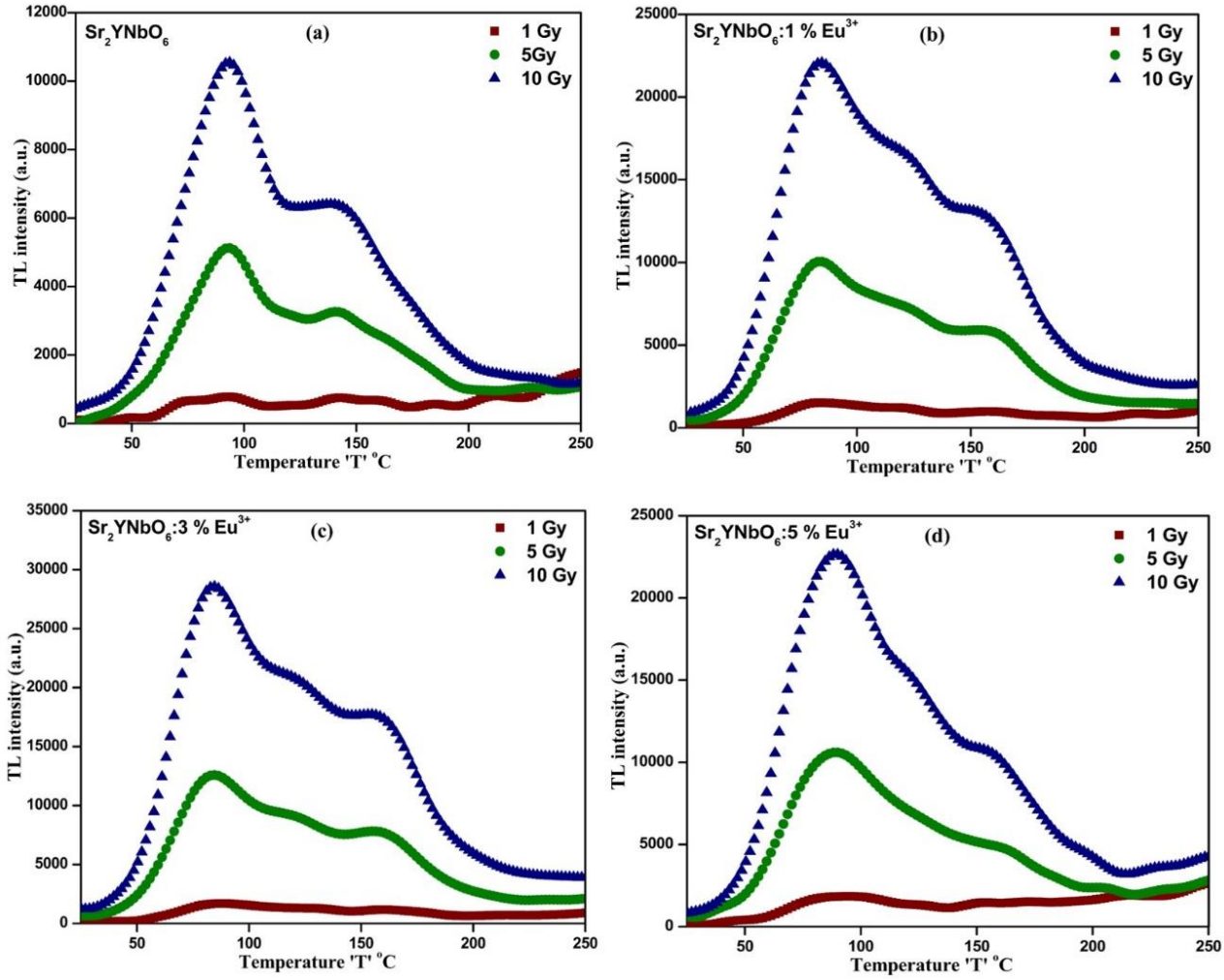

Figure 3.18. TL glow curves of Sr_2YNbO_6:x mol% Eu^{3+} (x=0, 1, 3, 5) phosphors at different beta doses.

In the present phosphor system, to understand the dose response towards high-energy beta rays, all TL investigated phosphors were irradiated with different doses of beta rays, mainly 1, 5, and 10 Gy. Figure 3.18 (a, b, c, d) illustrates the TL glow curves of Sr_2YNbO_6: Eu^{3+} phosphors at different beta doses. From the figures, a mixed TL peaks were found, for which the intensity is increases with increasing beta doses. The TL intensity exhibited a proportional increase as the beta radiation dose rose, indicating progressively increased traps upon continues ionization [49,50]. Table 3.9 shows all the observed TL peaks and their respective TL intensity counts.

Sr No.	Pure sample		Sr_2YNbO_6: 1% Eu^{3+}		Sr_2YNbO_6: 3% Eu^{3+}		Sr_2YNbO_6: 5% Eu^{3+}	
	Peak temp.	TL Intensity	Peak temp.	TL Intensity	Peak temp.	TL Intensity	Peak temp.	TL Intensity
1	94	10543	85	22067	85	28565	87	22641
2	142	6372	120	16468	120	20798	124	14797
3	-	-	155	12963	155	17713	156	10565

Table 3.9. TL peak temperature and their respective TL intensity counts after 10 Gy beta irradiation.

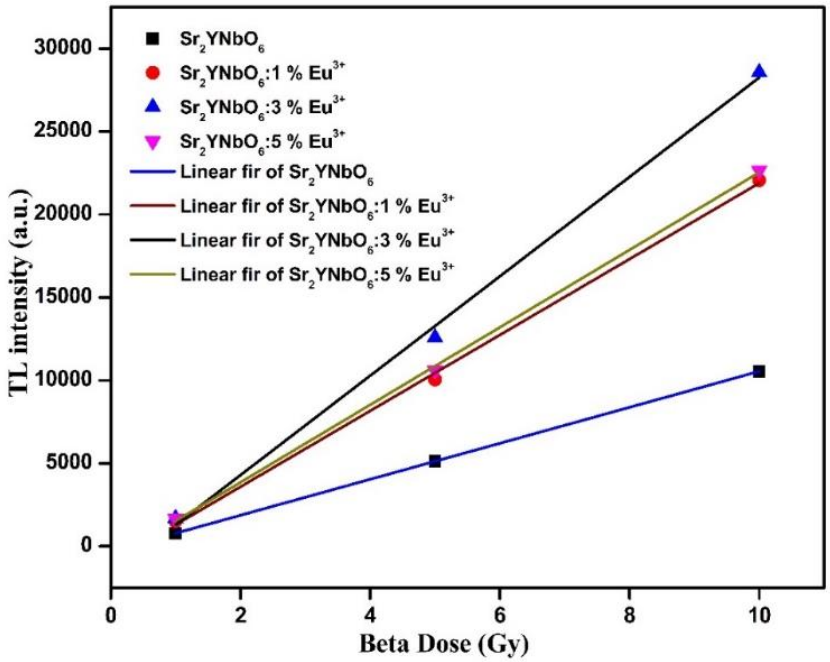

Figure 3.19. Dose response of Sr_2YNbO_6:x mol% Eu^{3+} (x=0, 1, 3, 5) phosphors towards beta rays.

As shown in Figure 3.19, a linear relationship among TL intensity and beta radiation dosage was observed within the dose of 1 and 10 Gy. The linear dose-response relationship between TL intensity and rising beta radiation doses demonstrated that the trapping centres improved proportionally with the absorption of ionizing radiation. The rise in TL intensity for the most intense glow peak is noticeable as the beta irradiation dose raised from 1 Gy to 10 Gy. This rise in TL glow is attributed to the rising population of trapping centres. From the figure 3.18 and Table 3.9, it is observed that the 3 mol% doped phosphors exhibited the highest intensity peaks for all

applied beta doses. Furthermore, the TL intensity of 1 mol% and 5 mol% Eu^{3+} doped phosphors is nearly the same [51,52].

The study of experimental TL glow curves provides an understanding of the trapping centres and associated kinetic parameters of generated traps. Various analysis techniques have been introduced to examine these experimental TL glow curves. Some widely used methods include the Chen's peak shape method (PSM), initial rise (IR) approach, the whole glow curve method, and computerized glow curve deconvolution (CGCD). These approaches are commonly employed for the glow curve analysis. Among these approaches, Chen's PSM and CGCD were taken into account, and the subsequent trapping parameters were determined.

The determination of trapping parameters becomes easier when the glow curve comprises an isolated peak; however, in the case of the glow curve containing overlapping glow peaks, finding trapping parameters is quite difficult. Consequently, the experimental TL glow curve requires deconvolution [53]. The CGCD method was employed to distinguish individual glow peaks from experimentally generated glow curves. To identify the nature of these deconvoluted glow peaks and ascertain their order of kinetics, Kitis et al. derived a set of equations [54]. This approach was applicable to all three order of kinetics. The corresponding mathematical expressions for all three order of kinetic are provided below:

Mathematical expression for first-order kinetics:

$$I(T) = I_M \exp\left[1 + \frac{E_a}{k_B T}\cdot\frac{T-T_M}{T_M} - \frac{T^2}{T_M^2}\times\left(1-\frac{2k_BT}{E_a}\right)exp\left(\frac{E_a}{k_BT}\cdot\frac{T-T_M}{T_M}\right) - \frac{2k_BT_M}{E_a}\right] \quad \text{..... (3.13)}$$

Mathematical expression for second-order kinetics:

$$I(T) = 4I_M exp\left(\frac{E_a}{k_BT}\cdot\frac{T-T_M}{T_M}\right)\times\left[\frac{T^2}{T_M^2}\cdot\left(1-\frac{2k_BT}{E_a}\right)exp\left(\frac{E_a}{k_BT}\cdot\frac{T-T_M}{T_M}\right) + 1 + \frac{2k_BT_M}{E_a}\right]^{-2} \quad \text{..... ... (3.14)}$$

Mathematical expression for general-order kinetics:

$$I(T) = I_M b^{b-1} exp\left(\frac{E_a}{k_BT}\cdot\frac{T-T_M}{T_M}\right)\times\left[(b-1)\frac{T^2}{T_M^2}\cdot\left(1-\frac{2k_BT}{E_a}\right)exp\left(\frac{E_a}{k_BT}\cdot\frac{T-T_M}{T_M}\right) + 1 + -1)\frac{2k_BT_M}{E_a}\right]^{-\frac{b}{b-1}} \quad \text{..... (3.15)}$$

Where, T_M temperature at maximum intensity I_M, T is the TL temperature points, k_B stands for the Boltzmann's constant, E_a is the trap depth, and b denotes order of kinetics.

Moreover, another trap parameter namely frequency factor (s) can also be computed by applying the CGCD method. The expressions to determine the frequency factor are as follow,

For first order kinetics,

$$s = \frac{\beta E_a}{k_B T_M^2} exp\left(\frac{E_a}{k_B T_M}\right) \quad \text{..... (3.16)}$$

For second order kinetics

$$s = \frac{\beta E_a}{k_B T_M^2\left(1+\frac{2kT_M}{E_a}\right)} exp\left(\frac{E_a}{k_B T_M}\right) \quad \text{..... (3.17)}$$

For general order kinetics

$$s = \frac{\beta E_a}{k_B T_M^2\left[1+\frac{2kT_M(b-1)}{E_a}\right]} exp\left(\frac{E_a}{k_B T_M}\right) \quad \text{..... (3.18)}$$

Where, all the notations have their usual meanings.

The good superposition of experimental and theoretical glow curves can be evaluated from a fitting parameter called figure of merit (FOM).

Following was the expression for FOM,

$$FOM = \frac{\sum_p |I_{Exp} - I_{Th}|}{\sum_p |I_{Th}|} \quad \text{..... (3.19)}$$

where, I_{exp} denotes the experimentally observed intensity counts of deconvoluted glow curves, whereas, I_{th} denotes theorical intensity counts.

In the present study, we found mixed peaks with various intensities in all the phosphors under study for different beta doses. The following are the GCD fittings of the 10 Gy dose beta irradiated undoped and Eu^{3+} doped phosphors under study.

From the deconvoluted TL glow curves, the acquired glow curves of the phosphor under study comprised three distinct glow peaks with a centre temperature of 83°C, 117°C, and 153 °C. Upon implementation of GCD, all three deconvoluted peaks identified above following second order kinetics, verified by the calculation of 'b' (order of kinetic factor). The calculated 'b' values were lie within 1.9-2.1 for the deconvoluted peaks identified above and are closely equal to the value of 'b' proposed by Kitis in the case of the glow curve following second-order kinetics [55,56]. The activation energies correspond to all deconvoluted peaks and were computed with the formula of activation suggested by Kitis et al. for the second-order kinetic glow peaks. The GCD determined kinetic parameters are tabulated in Table 3.10.

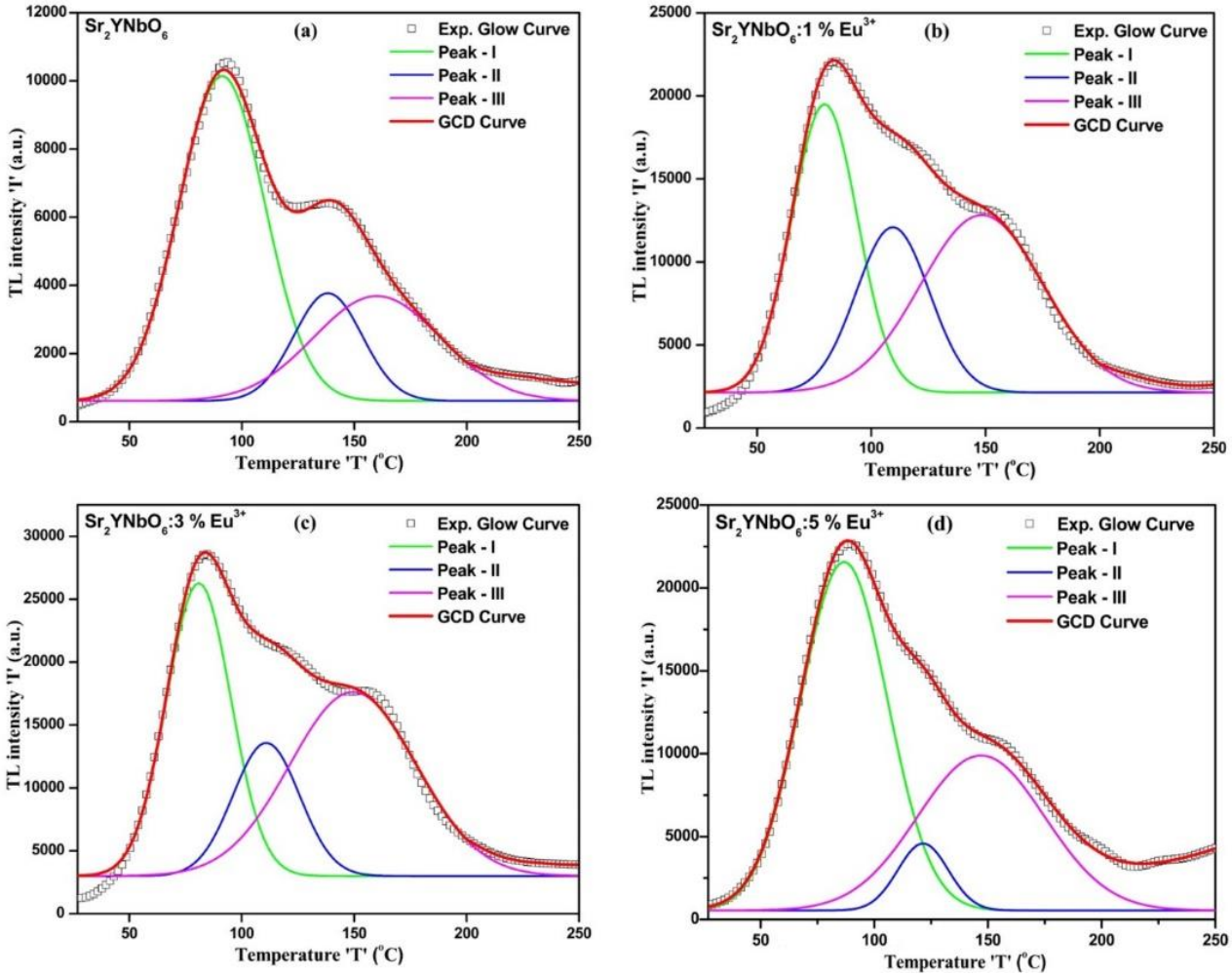

Figure 3.20. Deconvoluted TL glow curves of Sr_2YNbO_6:x mol% Eu^{3+} (x=0, 1, 3, 5) phosphors after beta irradiation of 10 Gy.

Furthermore, the PSM approach of trapping parameter determination was applied, and the same deconvoluted curves shown in Figure 3.20 were considered. In order to apply PSM, the first step involved deconvoluting the experimental TL glow curve. The process of deconvolution is crucial for identifying the trapping centres generated as a result of ionizing radiation exposure. Chen's energy equation was utilized to determine the trap depths and other associated trapping parameters of the deconvoluted curves within the experimental glow curve. Additionally, the determination of the order of kinetics can be achieved through the calculation of the geometrical factor, also referred to as the shape factor μ_g [57].

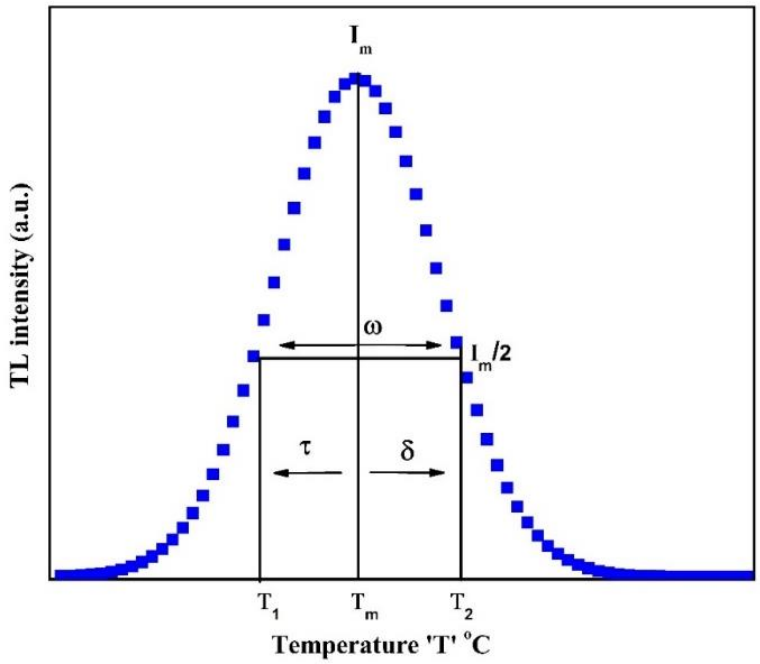

Figure 3.21. Notation of peak shape method.

Figure 3.21 depicts the notation for the PSM with necessary depictions. This method of trap parameter determination comprises a series of equations relating to several parameters, such as the full width at half intensity ($\omega = T_2 - T_1$), low temperature half width ($\tau = T_m - T_1$), and high temperature half width ($\delta = T_2 - T_m$). In this context, T_1 and T_2 denote the low and high temperatures corresponding to half of the prominent intensity of TL glow curve, while T_m represents the centre temperature at which the TL glow reaches its maximum. The calculation of trap depth utilized a general formula proposed by the Chen. The formula remains effective for any order kinetics followed by glow curve [58,59].

$$E = C_\alpha \left(\frac{k\,T_M^2}{\alpha}\right) - B_\alpha(2kT_M) \ldots\ldots\ldots\ldots\ldots\ldots\ldots\ldots\ldots\ldots\ldots\ldots (3.20)$$

Where α represents τ, δ, and ω respectively. The C_α and B_α can be computed using following expressions.

$$C_\tau = 1.51 + 3(\mu_g - 0.42) \qquad B_\tau = 1.58 + 4.2(\mu_g - 0.42)$$

$$C_\delta = 0.976 + 7.3(\mu_g - 0.42) \quad B_\delta = 0$$

$$C_\omega = 2.52 + 10.2(\mu_g - 0.42) \quad B_\omega = 1 \ldots\ldots\ldots\ldots\ldots\ldots\ldots (3.21)$$

Moreover, the geometrical factor ($\mu_g = \delta/\omega$) also called the shape factor, and was computed to examine the nature of the deconvoluted peaks identified in deconvoluted glow curve [60]. The determination of geometrical factor values was carried out based on the analysis of deconvoluted peaks. As a result, the calculated μ_g values lie within 0.51-0.52 for the deconvoluted peaks identified above and are closely equal to the value of μ_g proposed by Chen ($\mu_g = 0.52$) in the case of the glow curve following second-order kinetics [61,62]. As per GCD findings, the second order kinetics of the all three deconvoluted peaks were further supported by PSM method. The activation energies correspond to all deconvoluted peaks and were computed with the formula of activation suggested by the Chen for the second order kinetic glow peaks. The PSM determined kinetic parameters are tabulated in Table 3.11.

Sample		**I_{max}**	**T_{max} (K)**	**μ_g**	**Activation Energy (eV)**		
					E_τ	**E_δ**	**E_ω**
Sr_2YNbO_6	Peak-I	10143	363.7	0.52	0.79±0.03	0.81±0.04	0.80±0.02
	Peak-II	3772	410.7	0.51	1.19±0.06	1.20±0.06	1.20±0.04
	Peak-III	3688	432.2	0.51	0.63±0.02	0.71±0.02	0.67±0.01
Sr_2YNbO_6: 1 mol% Eu^{3+}	Peak-I	21193	354.9	0.52	0.86±0.04	0.86±0.04	0.86±0.03
	Peak-II	9211	389	0.51	1.26±0.08	1.25±0.08	1.26±0.04
	Peak-III	12753	423.4	0.52	0.76±0.02	0.79±0.03	0.78±0.02
Sr_2YNbO_6: 3 mol% Eu^{3+}	Peak-I	26200	353	0.51	0.96±0.05	0.96±0.06	0.96±0.03
	Peak-II	14247	383.25	0.51	0.94±0.05	0.97±0.05	0.96±0.03
	Peak-III	17544	423.2	0.51	0.61±0.02	0.70±0.02	0.66±0.01
Sr_2YNbO_6: 5 mol% Eu^{3+}	Peak-I	21579	359.2	0.51	0.73±0.03	0.78±0.04	0.75±0.02
	Peak-II	4580	394.5	0.51	1.72±0.14	1.71±0.14	1.72±0.07
	Peak-III	9891	419.6	0.51	0.68±0.02	0.76±0.03	0.72±0.01

Table 3.10. Summary of TL kinetic parameters calculated by PSM.

Sample		T_m (K)	Activation Energy 'E_a' (eV)	Order of Kinetics 'b'	FOM %	Frequency Factor 's' (s^{-1})
Sr_2YNbO_6	Peak-I	363.7	0.81±0.02	2.1	2.70	4.60×10^{10}
	Peak-II	410.7	1.16±0.06	2.1		4.70×10^{13}
	Peak-III	432.2	0.70±0.02	2.1		2.0×10^{7}
Sr_2YNbO_6: 1 mol% Eu^{3+}	Peak-I	354.7	0.85±0.02	2.0	3.08	1.70×10^{11}
	Peak-II	389	1.16±0.05	2.0		1.80×10^{14}
	Peak-III	423.5	0.80±0.03	2.1		2.70×10^{8}
Sr_2YNbO_6: 3 mol% Eu^{3+}	Peak-I	353	0.90±0.02	2.1	3.21	1.10×10^{12}
	Peak-II	383.24	1.07±0.06	1.9		1.30×10^{13}
	Peak-III	423.3	0.78±0.03	2.0		1.70×10^{8}
Sr_2YNbO_6: 5 mol% Eu^{3+}	Peak-I	359.2	0.78±0.03	2.1	2.64	1.20×10^{10}
	Peak-II	394.5	1.58±0.07	1.9		4.30×10^{19}
	Peak-III	419.6	0.75±0.01	2.1		8.50×10^{8}

Table 3.11. Summary of TL kinetic parameters calculated by GCD method.

References:

1. A. Mills, Phosphors development for LED lighting, *III-Vs Review* **18** (2005) 32-34.
2. M. Fang, Z. Bao, W. Huang et al., Evolutionary Generation of Phosphor Materials and Their Progress in Future Applications for Light-Emitting Diodes, *Chem. Rev.* **122** (2022) 11474-11513.
3. Z. Xia, Z. Xu, M. Chen et al., Recent developments in the new inorganic solid-state LED phosphors, Dalton Trans. 28 (2016) 11214-11232.
4. Y. Kim, N. Viswanath, S. Unithratti et al., Review-Phosphor Plates for High-Power LED Applications: Challenges and Opportunities toward Perfect Lighting, *ECS J. Solid State Sci. Tech.* **7** (2017) R3134.
5. N. Degda, N. Patel, V. Verma, K. V. R. Murthy, D. Harnath, M. Srinivas, Europium doped Sr_2YNbO_6 double perovskite phosphor for photoluminescence and thermoluminescence properties, *Luminescence* **38** (2023) 176-187.
6. J. Chen, S. Zhao, Z. Zhao et al., The structure and luminescence properties of blue-green-emitting Sr_2YNbO_6: Bi^{3+} phosphors, *J. Lumin.* **239** (2021) 118336.
7. L. Shi, Y. Han, Z. Ji et al., Effects of Al^{3+}-substitution on photoluminescence properties of Sr_2YNbO_6:Mn^{4+} far-red phosphor for plant cultivation, *J. Lumin.* **218** (2020) 116828.
8. C. Limberkar, A. Patel, K. Patel et al., Anisotropic study of photo-bolometric effect in $Sb_{0.15}Ge_{0.85}Se$ ternary alloy at low temperature, *J. Alloy. Comp.* **846** (2020) 156391.
9. C. Wei, D. Xu, J. Li et al., Synthesis and luminescence properties of Eu^{3+}-doped a novel double perovskite Sr_2YTaO_6 phosphor, *J. Mater. Sci: Mater. Electron.* **30** (2019) 2864-2871.
10. Z. Guo, Z. Zhu, X. Zhang et al., Photoluminescent properties and Judd-Ofelt analysis of Eu^{3+}-doped $NaMg(PO_3)_3$ red phosphor, *J. Lumin.* **202** (2018) 484-488.
11. N. Barot, P. Mehta, A. Rao et al., Effects of iso- and polyvalent substitutions on the short/long-range crystalline order in $CuCrO_2$ compounds, *J. Alloy. Comp.* **791** (2019) 134-143.
12. K. Patel, G. Solanki, K. Patel et al., X-ray Diffraction Analysis of Hexagonal Klockmannite CuSe Nanoparticles for Photodetectors under UV Light, *J. Phys. Chem. C* **125** (2021) 3517-3526.

13. G. Apsana, P. P. George, N. Devanna et al., Biomimetic Synthesis And Antibacterial Properties oif Strontium Oxide Nanoparticles Using Ocimum Sanctum Leaf Extract, *Asian J. Pharma. Clinic. Res.* **11** (2018) 384.

14. B. N. Lakshminarasappa, N. J. Shivaramu, K. R. Nagabhushana et al., Synthesis characterization and luminescence studies of 100 MeV Si^{8+} ion irradiated sol gel derived nanocrystalline Y_2O_3, *Nucle. Instru. Metho. Physi. Res. B.* **329** (2014) 40-47.
15. M. Srinivas, V. Verma, N. Patel et al., Characterization of newly synthesized Strontium Cerium Niobate nanophosphor, *J. Lumin.* **147** (2014) 324-327.
16. C. Bharti, A. Dutta, and T. P. Sinha, Modulus spectroscopy study of a double perovskite oxide Sr_2CeNbO_6: Frequency and time domain analyses, *Solid State Sci.* **14** (2012) 920-925.
17. F. Emen, V. Kafadar, N. Korozlu et al., The photoluminescence and thermoluminescence characteristics of the Eu^{3+} doped $CaMoO_4$: Detailed kinetic analysis of TL glow curves, *J. Lumin*. **222** (2020) 117130.
18. M. Im and Y. Kim, Energy transfer and multiple photoluminescence of $LuNbO_4$ co-doped with Eu^{3+} and Tb^{3+}, *Mater. Res. Bull*. **112** (2019) 399-405.
19. Y. Zhu, C. Tong, R. Dai et al., Luminescence properties of $Na_2Ca_2Si_3O_9$: Eu^{3+} phosphors via a sol-gel method, *Mater. Latter.* **213** (2018) 245-248.
20. F. Fan, L. Zhao, Y. Shang, Thermally stable double-perovskite Ca_3TeO_6:Eu^{3+} red-emitting phosphors with high color purity, *J. Lumin.* **211** (2019) 14-19.
21. S. Gupta, K. Sudarshan, A. Yadav et al., Deciphering the Role of Charge Compensator in Optical Properties of $SrWO_4$:Eu^{3+}:A (A = Li^+, Na^+, K^+): Spectroscopic Insight Using Photoluminescence, Positron Annihilation, and X-ray Absorption, *Inorg. Chem.* **57** (2018) 821-832.
22. J. Li, X. Wang, R. Cui et al., Synthesis and photoluminescence studies of novel double-perovskite phosphors, Ba_2GdTaO_6:Eu^{3+} for WLEDs, *Optik* **201** (2020) 163536.
23. H. Tseng, W. Tzou, S. Wei et al., Effects of synthesis temperature and Eu_2O_3 concentration on the crystalline phases and photoluminescence properties of $SrAl_2O_4$ phosphors, *J. Mater. Res. Technol.* **9** (2020) 14051-14060.

24. R. Krishnan, R. Kroon, and H. Swart, Charge transfer characteristics and luminescence properties of Eu^{3+} activated Ba_2YMoO_6 and $BaY_2(MoO_4)_4$ phosphors, *Mater. Res. Bull.* **145** (2022) 111554.
25. I. Nikiforov, D. Deyneko, D. Spassky et al., Tunable luminescence and energy transfer in Eu^{3+} doped $Ca_8MTb(PO_4)_7$ (M = Mg, Zn, Ca) phosphors, *Mater. Res. Bull.* **130** (2020) 110925.
26. R. Liu, Y. Zhan, L. Liu et al., Morphology analysis and luminescence properties of $YVO_4:Sm^{3+},Eu^{3+}$ prepared by molten salt synthesis, *Opt. Mater.* **100** (2020) 109633.
27. Z. Khan, N. Ingale and S. Omanwar, Combustion synthesis and luminescence studies of Eu (III) activated $LiBaBO_3$ inorganic phosphor, *Optik* **127** (2016) 9679-9682.
28. R. Cao, X. Lv, Y. Jiao et al., $Ca_3La_6Si_6O_{24}:Eu^{3+}$ orange-red-emitting phosphor: Synthesis, structure and luminescence properties, *Mater. Res. Bull.* **122** (2020) 110651.
29. Y. Parauha, and S. Dhoble, Synthesis and luminescence characterization of Eu^{3+}-doped $Ca_7Mg_2(PO_4)_6$ phosphor for eco-friendly white light-emitting diodes and thermoluminescence dosimetric applications, *Luminescence* **36** (2020) 1837-1846.
30. G. Kanmani, V. Ponnusamy, G. Rajkumar et al., Development of novel $Na_2Mg_3Zn_2Si_{12}O_{30}:Eu^{3+}$ red phosphor for white light emitting diodes, *Opt. Mater.* **96** (2019) 109350.
31. B. Zhang, J. Zhang, Y. Guo et al., Synthesis and photoluminescence of double perovskite $La_2LiSbO_6:Ln^{3+}$ (Ln=Eu, Tb, Tm, Sm, Ho) phosphors and enhanced luminescence of La2LiSbO6:Eu^{3+} red phosphor via Bi^{3+} doping for white light emitting diodes, *J. Alloy. Comp.* **787** (2019) 1163-1172.
32. Y. Tian, Development of phosphors with high thermal stability and efficiency for phosphor-converted LEDs, *J. Sol. State Light* **1** (2014) 11.
33. G. Rajkumar, V. Ponnusamy, G. Kanmani et al., A new perovskite type Ba_2YZrO_6: Eu^{3+} red phosphor with cubical morphology for WLEDs applications, *J. Lumin.* **227** (2020) 117561.
34. S. Zhang, Y. Nakai, T. Tsuboi et al., Luminescence and Microstructural Features of Eu-Activated $LiBaPO_4$ Phosphor, *Chem. Mater.* **23** (2011) 1216-1224.

35. D. Zhao, S. Zhang, Y. Fan et al., Thermally Stable Phosphor $KBa_2(PO_3)_5:Eu^{2+}$ with Broad-Band Cyan Emission Caused by Multisite Occupancy of Eu^{2+}, *Inorg. Chem.* **59** (2020) 8789-8799.
36. Y. Jia, D. Xu, X. Yun et al., Luminescence properties of high thermal stability $Sr_2ScTaO_6:Ln^{3+}$ (Ln^{3+}=Sm^{3+}/Dy^{3+}) phosphors with novel double perovskite structures, *Optik* **225** (2021) 165865.
37. X. Chen, Q. Xu, F. Hussain et al., High Thermal Stability and Color Purity of $Y_2SrAl_4SiO_{12}$: Eu^{3+} Garnet-Variant-Structured Phosphor for Warm White Light LED-Lamp, *Crystal* **12** (2022) 1382.
38. H. Lai, R. Yang and S. Chang, Thermally stable luminescence properties and energy transfer of green-emitting $LiBaPO_4:Tb^{3+},Ce^{3+}$ Phosphor, *Cera. Inter.* ***43*** (2017) S688-S693.
39. C. Zhao, Z. Xia and S. Yu, Thermally stable luminescence and structure evolution of (K, Rb)$BaPO_4:Eu^{2+}$ solid-solution phosphors, *J. Mater. Chem. C* **2** (2014) 6032-6039.
40. E. Huerta, I. Padilla, R. Martinez-Martinez et al., Extended decay times for the photoluminescence of Eu^{3+} ions in aluminum oxide films through interaction with localized states, *Opt. Mater.* **34** (2012) 1137-1142.
41. Y. Cai, Y. Yang, H. Liu et al., Synthesis of the Red-Emitting (Ba, $Ca)_2ScAlO_5:Eu^{3+}$ Phosphors with Photoluminescence Properties, *Inorg. Chem.* **61** (2022) 8529-8539.
42. N. Bhagya, P. Prashanth, R. Hari Krishna et al., Photoluminescence studies of Eu^{3+} activated $SrTiO_3$ nanophosphor prepared by solution combustion approach, *Optik* **145** (2017) 678-687.
43. V. Dubey, J. Kaur, S. Agrawal et al., Effect of Eu^{3+} concentration on photoluminescence and thermoluminescence behavior of $YBO_3:Eu^{3+}$ phosphor, *Superlattices Microstruc.* **67** (2014) 156-171.
44. B. Singh, Maheshwary, P. Ramakrishna et al., Improved photo-luminescence behaviour of Eu^{3+} activated $CaMoO_4$ nanoparticles via Zn^{2+} incorporation, *RSC Adv.* **5** (2015) 55977-55985.
45. C. Huerta-Rivera, R. Bernal, C. Cruz-Vazquez et al., Beta particle excited thermoluminescence of $CaZrO_3$ phosphors synthesized by solid state reaction, *Appl. Radia. Isotop.* **168** (2021) 109519.

46. H. Yazan, Z. Portakal-Ucar, S. Akca et al., Thermoluminescence of Ce and Nd co-doped CaF2 phosphors after beta irradiation, *J. Lumin.* **234** (2021) 117949.
47. A. Jadhaw, V. Sonwane, A. Gour et al., Thermoluminescence properties of Eu-doped and Eu/Dy-codoped $Sr_2Al_2SiO_7$ phosphors, *Luminescence* **32** (2017) 1349-1353.
48. Y. Halefoglu, M. Oglakci, Z. Portakal et al., A study on thermoluminescence behaviour of Eu doped LaB3O6 irradiated with beta particles, *Radia. Phys. Chem.* **168** (2020) 108571.
49. S. Akca, M. Oglakci, Z. Portakal et al., Thermoluminescence analysis of beta irradiated ZnB2O4: Pr3+ phosphors synthesized by a wet-chemical method, *Radia. Phys. Chem.* **160** (2019) 105-111.
50. U. Kaynar, S. Kaynar, Y. Alajlani et al., Eu^{3+} and Dy^{3+} doped La_2MoO_6 and $La_2Mo_2O_9$ phosphors: Synthesis and luminescence properties, *Mater. Res. Bull.* **123** (2020) 110723.
51. S. Kaur, A. Rao, M. Jayasimhadri et al., Synthesis optimization, photoluminescence and thermoluminescence studies of Eu^{3+} doped calcium aluminozincate phosphor, *J. Alloy. Comp.* **802** (2019) 129-138.
52. H. Lokesha, N. Chauhan, K. Nagabhushana, et al., Dosimetric properties of ZrO_2 and ZrO_2:Sm^{3+} exposed to beta rays, *Cera. Inter.* **44** (2018) 18871-18877.
53. J. Benavente, J. Gomez-Ros and A. Romero, Thermoluminescence glow curve deconvolution for discrete and continuous trap distributions, *Appl. Radia. Isotop.* **153** (2019) 108843.
54. G. Kitis, J. Gomez-Ros and J. W. N. Tuyn, Thermoluminescence glow-curve deconvolution functions for first, second and general orders of kinetics, *J. Phys. D: Appl. Phys.* **31** (1998) 2636.
55. N. Shivaramu, B. Lakshminarasappa, K. Nagabhushana et al., Photoluminescence, thermoluminescence glow curve and emission characteristics of Y_2O_3:Er^{3+} nanophosphor, *Spectr. Acta Part A: Molec. Biomolec. Spectro.* **189** (2018) 249-356.
56. I. Charak, M. Manhas, P. Khajuria et al., Investigation of thermoluminescence response and kinetic parameters of $CaMgB_2O_5$:Tb^{3+} phosphor against UV-C radiation for dosimetric application, *J. Mater. Sci.: Mater. Electron.* **32** (2021) 17418-17426.
57. G. Kitis, R. Chen and V Pagonis, Thermoluminescence glow-peak shape methods based on mixed order kinetics, *Phys. Status Solidi (a)* **205** (2008) 1181-1189.

58. A. Kadam, G. Mishra and S. Dhoble, Thermoluminescence study and evaluation of trapping parameters $CaTiO_3$: RE (RE=Eu^{3+}, Dy^{3+}) phosphor for TLD applications, *J. Molec. Struct.* **1225** (2021) 129129.
59. S. Dhas, S. Suresh, A. Rita et al., Effect of annealing on the photoluminescence and thermoluminescence properties of Eu^{2+} doped $BaSO_4$ microgravels, *J. Mater. Sci: Mater. Electron.* **31** (2020) 11113-11122.
60. R. Neema, M. Saleem, P. Sharma et al., Luminescence Studies of rare-earth Ce^{3+} and Dy^{3+} doped $SrAl_2O_4$ aluminate phosphors, *J. Mater. Sci: Mater. Electron.* **32** (2021) 12318-12329.
61. K. Gavhane, M. Bhadane, P. Kulkarni et al., Investigation of novel Eu doped $SrDy_2O_4$ microphosphor for thermoluminescence dosimetry, *J. Lumin.* **231** (2021) 117781.
62. J. Kalita and M. Chithambo, Structural, compositional and thermoluminescence properties of microcline ($KAlSi_3O_8$), *J. Lumin.* **224** (2020) 117320.